

OARnet: Automated organs-at-risk delineation in Head and Neck CT images

Mumtaz Hussain Soomro¹, Hamidreza Nourzadeh^{1,2}, Victor Gabriel Leandro Alves¹,
Wookjin Choi^{1,3}, Jeffrey V. Siebers¹

¹University of Virginia Health System, Charlottesville, VA

²Thomas Jefferson University Hospital, Philadelphia, PA

³Virginia State University, Petersburg, VA

Objective: To auto-delineate organs-at-risk (OARs) in head and neck (H&N) CT image sets via a compact high-performance knowledge-based model.

Approach: A 3D deep learning model (OARnet) is developed and used to delineate 28 H&N OARs on CT images. OARnet utilizes a densely connected network to detect the OAR bounding-box, then delineates the OAR within the box. It reuses information from any layer to subsequent layers and uses skip connections to combine information from different dense block levels to progressively improve delineation accuracy. Training uses up to 28 expert manual delineated (MD) OARs from 165 CTs. Dice similarity coefficient (DSC) and the 95th percentile Hausdorff distance (HD95) with respect to MD is assessed for 70 other CTs. Mean, maximum, and root-mean-square dose differences with respect to MD are assessed for 56 of the 70 CTs. OARnet is compared with UaNet, AnatomyNet, and Multi-Atlas Segmentation (MAS). Wilcoxon signed-rank tests using 95% confidence intervals are used to assess significance.

Results: Wilcoxon signed ranked tests show that, compared with UaNet, OARnet improves ($p<0.05$) the DSC (23/28 OARs) and HD95 (17/28). OARnet outperforms both AnatomyNet and MAS for DSC (28/28) and HD95 (27/28). Compared with UaNet, OARnet improves median DSC up to 0.05 and HD95 up to 1.5mm. Compared with AnatomyNet and MAS, OARnet improves median (DSC, HD95) by up to (0.08, 2.7mm) and (0.17, 6.3mm). Dosimetrically, OARnet outperforms UaNet (D_{\max} 7/28; D_{mean} 10/28), AnatomyNet (D_{\max} 21/28; D_{mean} 24/28), and MAS (D_{\max} 22/28; D_{mean} 21/28).

Conclusion: A compact method for OAR auto-delineation using modern deep-learning methods is described and applied to H&N auto-delineation. The DenseNet architecture is optimized using a hybrid approach that performs OAR-specific bounding box detection followed by feature recognition. Compared with other auto-delineation methods, OARnet is better than or equal to UaNet for all but one geometric (Temporal Lobe L, HD95) and one dosimetric (Eye L, mean dose) endpoint for the 28 H&N OARs, and is better than or equal to both AnatomyNet and MAS for all OARs.

Keywords: Computer tomography (CT), head and neck (H&N), auto-delineation, deep learning, radiotherapy treatment planning.

1 Introduction

Accurate delineation of organs-at-risk (OARs) is considered to be a crucial step in Head and Neck (H&N) radiation therapy treatment planning to ensure adverse consequences to healthy surrounding organs are minimized [1]. Erroneous OAR delineation can affect the desired dose distribution and, consequently, the treatment outcome. Typically, OARs are manually delineated by radiation oncology experts. The manual delineation process is time-consuming and laborious [2], presents inter-and intra-observer variability [3], [4], and is inapt for fully automated treatment planning. Auto-delineation of H&N OARs is challenging because, across the many OARs that requiring delineation, there is inconsistent behavior in terms of size, shape, and image intensity, thereby posing challenges to delineation software. Automated OAR delineation may be beneficial if the resultant delineations are sufficiently accurate for the clinical task, and the creation of such delineations, including required delineation review and adjustment, improves clinical efficiency.

Many automated delineation methods have been proposed. Atlas-based auto-delineation (ABAS) of H&N CT images has been widely explored [5]–[8]. ABAS consists of four major processing tasks: (i) pre-processing; (ii) atlas creation; (iii) patient registration (mostly with deformation) and; (iv) label fusion. ABAS uses these steps to transfer delineations from the reference (atlas) set to the case under consideration [9]. Although ABAS is used for radiotherapy treatment planning auto-delineating, it has shortcomings; e.g., it has poor performance for thin or small OARs [5], and it inadequately copes with inter-patient anatomic variation, particularly from the fixed atlas set [10]. Learning-based ABAS are designed to directly delineate OARs without aligning the new patient to the fixed reference atlas [7], [11]; such methods involve preprocessing jobs and extraction of handcrafted features that could lead to sub-optimal performance. Learning-based ABAS techniques are computationally expensive.

Recently, deep learning – artificial intelligence (AI) – based convolutional neural networks (CNNs) methods have been successfully applied with impressive results for medical image delineation [12]–[18], [19]. Unlike atlas-based methods, deep learning-based approaches learn features of the intricate patterns and structures from large, well-organized training datasets that are used to train the model based upon prior information. Subsequently, the trained model is applied to new unseen data for prediction without aligning or registering the new data to an atlas or template. Current deep learning-based methods have been applied to auto-delineate anatomical structures in H&N CT images [20]–[28]. [29], [30], [31].

Many methods are patch-based to circumvent GPU memory constraints, wherein preprocessing crops random image regions near the OAR/region of interest (ROI) from the CT image. It has been shown that patched-based methods yield false-positive delineations [29], [30], [31].

Among AI methods, Zhu et al. [30] developed AnatomyNet, a 3D Unet [13] based network that directly yields OARs delineations from a whole-volume H&N CT scan without laborious local patch cropping preprocessing. AnatomyNet gave better accuracy in delineating large OARs than delineating small OARs. Wang et al. [32] proposed a two-stage 3D Unet OAR delineation framework to separately delineate large and small OARs, where the 3D Unet was dedicated to complete each stage's task. The first stage automatically approximated the OAR's initial size and location with a bounding box, and the second stage performed the delineation within a bounding box. The 3D Unet for both [30], [32] consists of an encoder and decoder architecture with skip connections concatenating low high-level features of the same resolution in both the encoder and decoder. The 3D Unet method simultaneously learns low- and high-level information, which has been proven efficacious for accurate biomedical image delineation. However, the 3D Unet results in some inaccurate delineations, which may be clinically unacceptable [31]-[33], [34]. Also, these studies fail to delineate some in-field-of-view OARs.

While the 3D Unet methods mentioned above can maximize the gradient from the encoder to the decoder, they do not maximize the gradient from layer to layer. Addressing this, Tang et al. [31] proposed an attention-modulated Unet (UaNet) to delineate 28 H&N OARs. UaNet is also a two-stage framework. The first stage is an OAR detection. The actual size and location of each OAR are approximated in a bounding box. The second stage is an OAR delineation, where the detected OAR is segmented. UaNet uses ResNet [33], [35] in the encoder to maximize the bounding box detection and OAR delineation accuracy.

Additionally, ResNet maximizes the gradient layer to layer by adding the previous layer's features to the next, but the addition of these features makes the network complex. Huang et al. [34] presented densely connected convolutional networks (DenseNet), an extension of the reusing feature concept from [12], [35], by building direct connections from every layer to the corresponding previous layers to ensure maximum gradient flow between layers. DenseNet has demonstrated effective performance and attained consistent improvement over ResNet in 2D natural image classification. Considering the success of DenseNet, Yu et al. [15] introduced DenseVoxNet, a 3D version of DenseNet for volumetric cardiac segmentation. DenseVoxNet utilizes two dense blocks followed by pooling layers which learn high-level resolution features in the first block and low-level resolution features in the second. The high-resolution features are restored by incorporating stacks of learnable deconvolution layers. There is no direct connection between dense blocks and final predictions that discards multi-scale contextual information, thereby reducing delineation accuracy [36].

The multi-scale contextual information is useful for producing accurate delineation. In this regard, Bui et al. [37] proposed a novel end-to-end 3D DenseNet for segmenting volumetric infant brain MRI,

named 3D-SkipDenseSeg. 3D-SkipDenseSeg introduced skip-connection between dense blocks and the final prediction. In this way, the network yields accurate delineation by learning multi-contextual information throughout the network.

Building on the developments described above, this work develops a novel clinically applicable deep learning framework based on a densely connected network to accurately delineate each OAR in head and neck CT images. Our network, OARnet, follows a 3D-SkipDenseSeg flow. In contrast to state-of-art models (particularly 3D Unet and ResNet-based), our method of using skip-connection (Figure 1) does not increase the number of learnable parameters, reduces required memory resources, and avoids over-fitting.

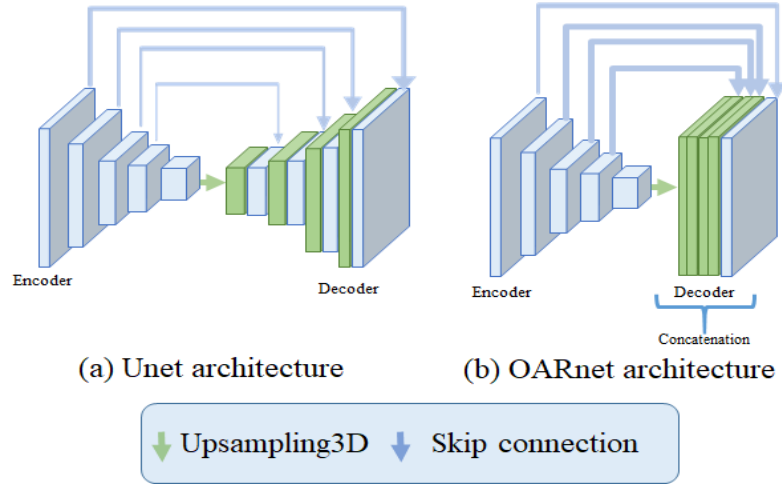


Figure 1 A comparison between Unet and OARnet architectures. The Unet figure is modified from [37].

Figure 1 demonstrates the main difference between the Unet architecture (2D Unet [12], 3D Unet [13]) and the OARnet architecture. The Unet uses the stacked deconvolution layers where the encoder's low-level resolution features are progressively up-sampled and then concatenated with high-level features of decoder. Each decoder level raises the number of trainable parameters. In contrast, OARnet directly restores the low-level features to the same size as the input features and concatenates them together with the input features, thus requiring fewer trainable parameters than the Unet architecture.

2 Material and Methods

We utilized 235 publicly available H&N CTs from two different sources: 83 datasets from Head-Neck-cetuximab (HNC) [38] and 152 datasets Head-Neck-PET-CT (HNPETCT) [39]. Each dataset has up to 28 structures manually delineated by medical experts, which we use as the reference delineations. Among the 235 datasets, 165 (66 from HNC and 99 from HNPETCT) are used for

training and 70 (17 from HNC and 53 from HNPETCT) for assessment. A flowchart of data division is depicted in Figure 2. Data augmentation is utilized to enrich the data size and improve the deep learning-based algorithm results.

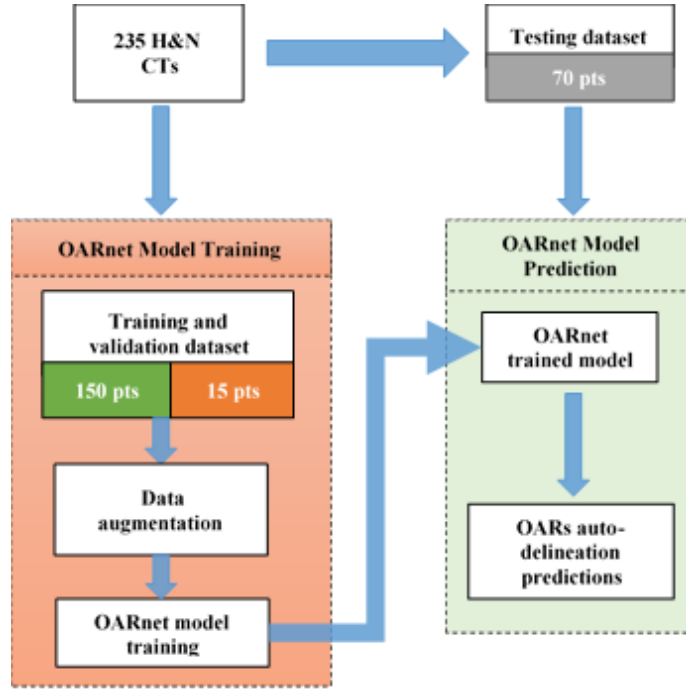


Figure 2 Flow of the two stages of the OARnet auto-delineation method.

The dimensions of the CT image sets used for the network are $512 \times 512 \times N$, where N is the number of slices that vary from patient to patient. The manually delineated structures include the seven typical H&N OARs (brainstem, left and right parotids, larynx, mandible, oral cavity, spinal cord) as well as twenty-one other potential OARs (brachial plexus, pharyngeal constrictor muscle, left and right inner ears, left and right eyes, left and right lenses, left and right optic nerves, left and right submandibular glands (SMG L & SMG R), left and right temporal lobes, left and right temporomandibular joints (TMJ L & TMJ R), hypophysis, optic chiasm, sublingual gland, thyroid, and trachea.

Figure 3 overviews the OARnet method; details are provided in the supplementary material. OARnet incorporates the densely connected network's characterization to delineate OARs in H&N CT images with 3D volume-to-volume learning. OARnet is comprised of three stages:

- I. **Encoder**, where the high-level features (i.e., feature map 1 as shown in Figure 3) and low-resolution features (i.e., feature map 2 and feature map 3) from three different dense blocks are extracted. OARnet follows the general 3D-SkipDenseSeg [37] architecture to extract the features.
- II. **Bounding box detection**, where each OAR is classified and its corresponding bounding box is predicted. This module follows Fast RCNN architecture [40]. The bounding detection

module takes the final feature map (i.e., feature map 3, as shown in Figure 3) and follows a two-way procedure – one is for OAR classification, and the other is predicting the bounding box for the classified OAR.

- III. **Decoder**, where the encoder's features are cropped using the predicted bounding box of classified OAR, upsampled and concatenated together.

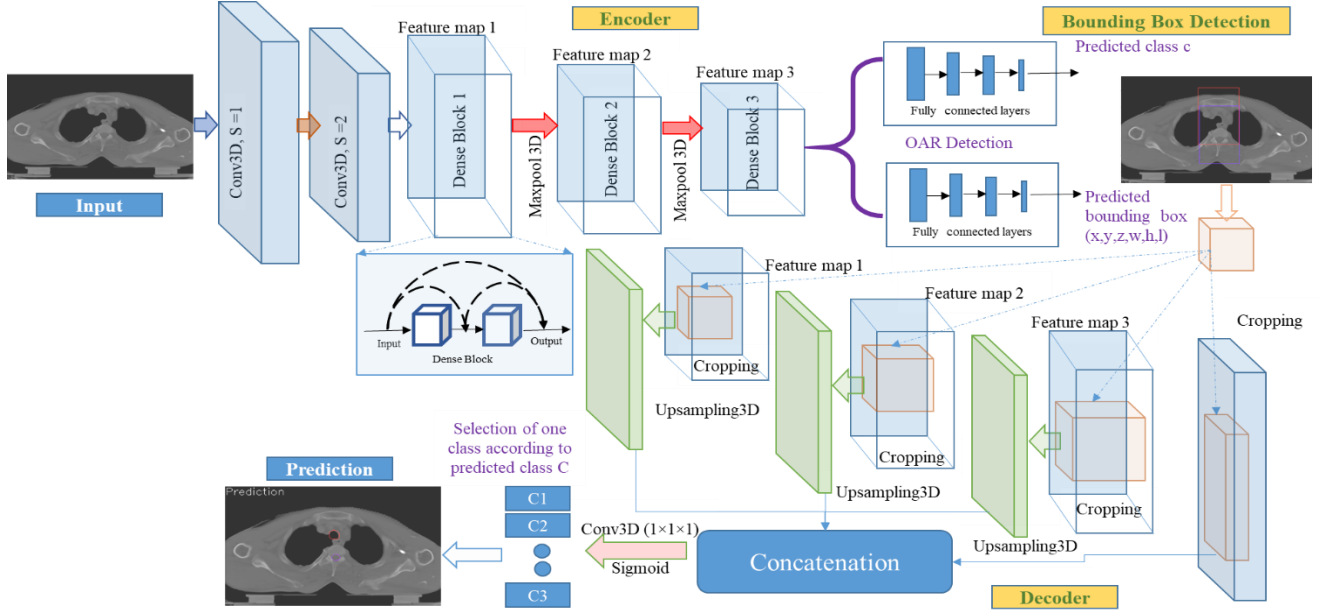


Figure 3 Architecture of OARnet, a densely-connected network for OAR delineation of CT images with 3D volume-to-volume learning.

OARnet was compared with Multi-Atlas Segmentation (MAS) [7], [8], [9], [10] as well as UaNet [31] and AnatomyNet [30] deep learning-based methods in its ability to reproduce the reference delineations. Previous studies have already shown that UaNet and AnatomyNet outperform traditional atlas-based approaches [7], [8], [9], [10]. For a fair and consistent comparison, all deep learning-based models were trained with hybrid loss function comprising a combination of Dice loss and focal loss, $\mathcal{L} = \mathcal{L}_{Dice} + \lambda_i \mathcal{L}_{Focal}$, following AnatomyNet's training procedure [30]. The Dice loss deals with lessening the imbalance voxel problem in the OARs class distribution where voxel-wise weights λ_i are applied to the loss function for combating the high dominance of the background class over smaller organs by assigning more weight to them [30].

The focal loss deals with reducing the voxels' misclassification. We trained the network on 200 epochs in total, where OAR candidates have been screened in the first 40 epochs and classified in the next five epochs. The OAR delineation network was trained in the final 155 epochs. We trained the network using Adam optimizer [41] with an initial learning rate set to 0.001, an L2 penalty set to 0.0001, and a batch size of one.

Each delineation method is intercompared with the reference delineations using geometric and dosimetric similarity analysis. Geometric similarity analysis utilized the volumetric Dice similarity coefficient (DSC) [42] and 95th percentile of the Hausdorff distance (HD) [43].

The DSC calculates volumetric overlap between the given reference delineation ground truth mask and the predicted output mask, and expressed as

$$DSC(M_p, M_r) = \frac{2|M_p \cap M_r|}{|M_p| + |M_r|}, \quad (1)$$

where M_p is the predicted delineation mask output, and M_r is the ground-truth reference delineation mask. DSC provides values between 0 and 1, where 1 indicates that the predicted delineation is identical to the reference delineation.

The HD is the maximum distance between the sets of boundary voxels of the predicted and reference delineations. HD mathematically is given as,

$$HD(M_p, M_r) = \max(h(M_p, M_r), h(M_r, M_p)), \quad (2)$$

where $h(M_p, M_r)$ is known as the directed HD and defined as

$$h(M_p, M_r) = \max_{a \in M_p} \min_{b \in M_r} \|a - b\|, \quad (3)$$

where a and b are the set of boundary points of M_p and M_r , respectively, and $\|a - b\|$ is the Euclidean distance between the points. As HD is highly sensitive to outliers, its 95th percentile is commonly used instead. Therefore, we used the 95th percentile Hausdorff distance ($HD95$).

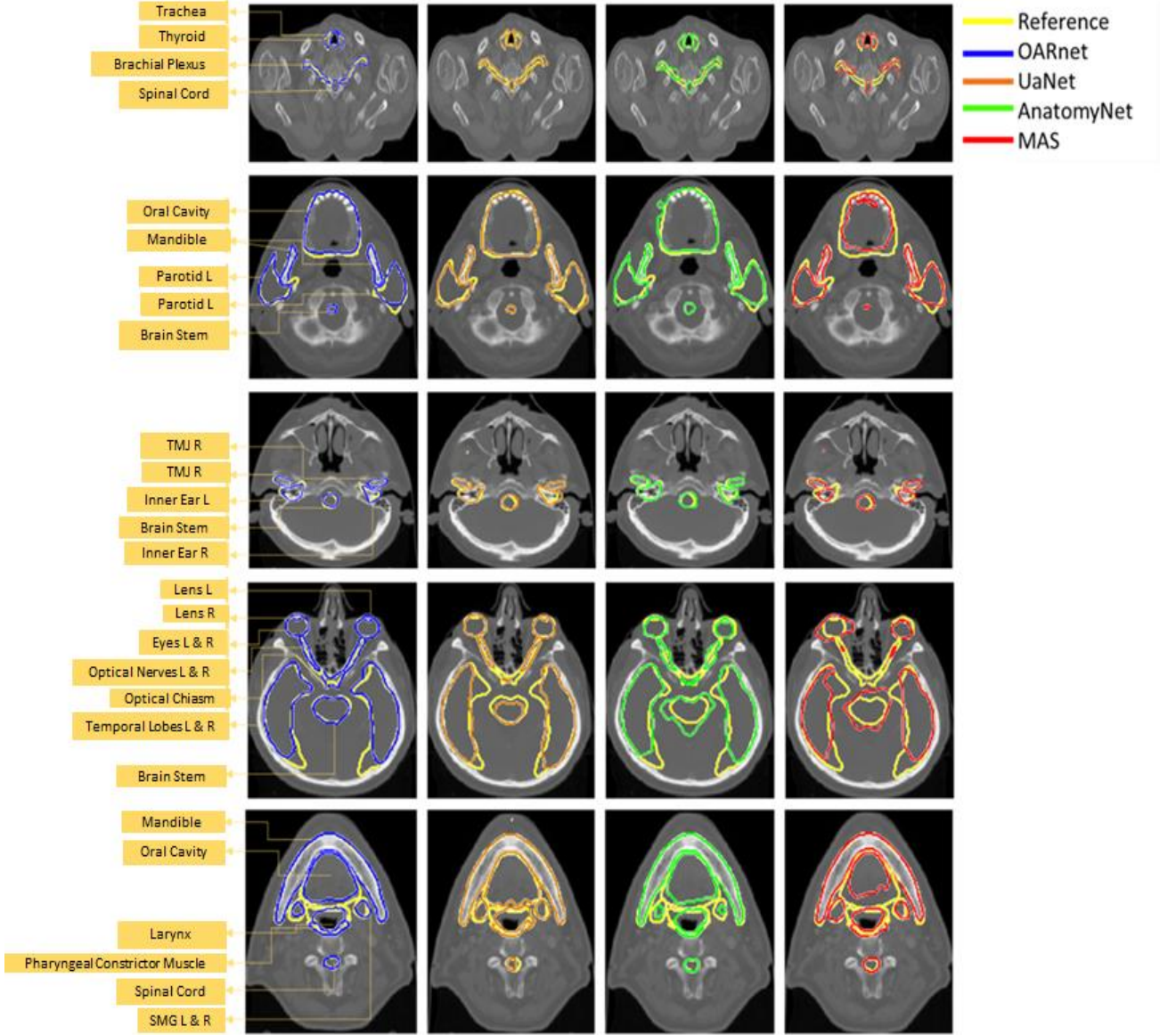


Figure 4 Visual comparisons among alternative delineation method results for a sample patient. The reference (yellow) is given in each panel.

Geometric similarity evaluations do not reveal the appropriateness of the delineations for the task of clinical radiation therapy dose assessment. Therefore, we utilize the delineations for dose assessment for an unseen 56 patients' image sets.

As complete dose difference assessment is cumbersome, like [44], we restrict comparisons to difference in the absolute mean and absolute max dose with respect to the reference delineations ($|\Delta D_{mean}|$ and $|\Delta D_{max}|$). These differences (residuals) indicate how close the delineation model is to the expected dose for the reference delineations near clinical doses of interest.

Wilcoxon signed-rank test for significance is computed for comparing each alternative method's performance with OARnet. The gain or loss distribution (*GoL*) of OARnet versus the alternative auto-delineation algorithms for *DSC*, *HD95*, and dose differences is also evaluated. The *GoL* functions are

defined as differences such that zero indicates equivalence, positive values indicate OARnet improvement (gain), and negative values indicate OARnet degradation (loss). Mathematically, the values are defined as:

$$GoL_{DSC}(OAR) = DSC(OAR, M_{OARnet}, M_r) - DSC(OAR, M_{alternative}, M_r) \quad (4)$$

$$GoL_{HD95}(OAR) = HD95(OAR, M_{alternative}, M_r) - HD95(OAR, M_{OARnet}, M_r) \quad (5)$$

$$GoL_{\Delta D_x}(OAR) = |\Delta D_x(D_{x,alternative}, D_{x,r})| - |\Delta D_x(D_{x,OARnet}, D_{x,r})| \quad (6)$$

The sample the root-mean-square error was computed for every OAR since RMS penalizes methods that produce poor delineations, yielding high dose deviation when compared to the reference.

3 Results

OARnet delineations are visually compared with the reference and alternative auto-delineations on a sample CT set in Figure 4. For this case, MAS was ineffective to yield delineations for the lens L, lens R, optical chiasm, optical nerve L, optical nerve R, and brachial plexus. OARnet, UaNet, and AnatomyNet visually reproduce the manually delineated reference OARs within several *mm*.

Table 1 shows one-sided Wilcoxon signed ranked tests comparing OARnet with the alternative delineation methods for *DSC* and *HD95* for all 28 delineations. Statistically significant values ($p < 0.05$) are indicated with a *. compares the *DSC* and *HD95* for seven typical clinically relevant OARs, while shows the *GoL* distributions for those quantities. Comparisons for other OARs are provided in the supplementary material.

One-sided Wilcoxon tests comparing OARnet to UaNet show that OARnet improves ($p < 0.05$) *DSC* for 23 out of 28 OARs and *HD95* for 17 out of 28 OARs. The opposite-sided Wilcoxon tests for *DSC* and *HD95* (not shown) find that UaNet improves *HD95* for 1 out of 28 OARs with $p < 0.05$ (Temporal Lobe L). Therefore, compared with UaNet, OARnet yields better than or equivalent *DSC* for all OARs, and better than or equal *HD95* for 27/28 OARs. Compared with UaNet, OARnet improves the median *DSC* up to 0.05 ((a)), and *HD95* by up to 1.5 mm ((d)).

OARnet outperformed both AnatomyNet and MAS for 28/28 OARs on *DSC* and 27/28 on *HD95* ($p < 0.05$). OARnet improves median *DSC* up to 0.08 and the median *HD95* up to 2.7 mm compared to AnatomyNet, respectively ((b) and (e)). Compared with MAS, median *DSC* improved by up to 0.17 and median *HD95* by up to 6.3 mm (Figure 6 (c) and (f)).

Table 1. One sided Wilcoxon signed-rank test p -values comparing alternative methods with respect to OARnet for geometric metrics which indicate similarity to the reference delineations. The null hypothesis is that the results are the same distribution. Statistically significant results with p -value < 0.05 , marked with a *, indicate a preference for OARnet (higher DSC, lower HD95). The last two rows indicate the number of OARs in which OARnet or the alternative delineation method (UaNet, AnatomyNet, MAS) metric achieved statistical significance ($p < 0.05$). Per-OAR and per-delineation method results for the opposite-sided tests (e.g. UaNet-OARnet) are not shown due to the sparsity of the significant results.

* p -value < 0.05	DSC - Wilcoxon signed rank test - OARnet greater than other methods			HD95 - Wilcoxon signed rank test - OARnet less than other methods		
OARs	OARnet - UaNet (p -value)	OARnet - AnatomyNet (p -value)	OARnet - MAS (p -value)	OARnet - UaNet (p -value)	OARnet - AnatomyNet (p -value)	OARnet - MAS (p -value)
Brachial Plexus	*	*	*	*	*	*
Brain Stem	*	*	*	*	*	*
Pharyngeal Constrictor Muscle	*	*	*	0.25	*	*
Inner Ear L	*	*	*	*	*	*
Inner Ear R	*	*	*	*	*	*
Eye L	*	*	*	0.08	*	*
Eye R	*	*	*	0.17	*	*
Hypophysis	*	*	*	*	*	*
Larynx	0.06	*	*	0.09	*	*
Lens L	*	*	*	0.30	*	*
Lens R	*	*	*	*	*	*
Mandible	*	*	*	0.50	*	*
Optical Chiasm	*	*	*	*	*	*
Optical Nerve L	*	*	*	*	*	*
Optical Nerve R	*	*	*	*	*	*
Oral Cavity	0.75	*	*	0.39	*	*
Parotid L	*	*	*	*	*	*
Parotid R	*	*	*	*	*	*
SMG L	*	*	*	*	*	*
SMG R	*	*	*	*	*	*
Spinal Cord	*	*	*	*	*	*
Sublingual Gland	0.19	*	*	0.31	*	*
Temporal Lobe L	0.51	*	*	1.00	0.14	0.31
Temporal Lobe R	0.06	*	*	0.81	*	*
Thyroid	*	*	*	*	*	*
TMJ L	*	*	*	*	*	*
TMJ R	*	*	*	*	*	*
Trachea	*	*	*	0.07	*	*
N - OARnet - p -value < 0.05	23	28	28	17	27	27
N - other method - p -value < 0.05	0	0	0	1	0	0

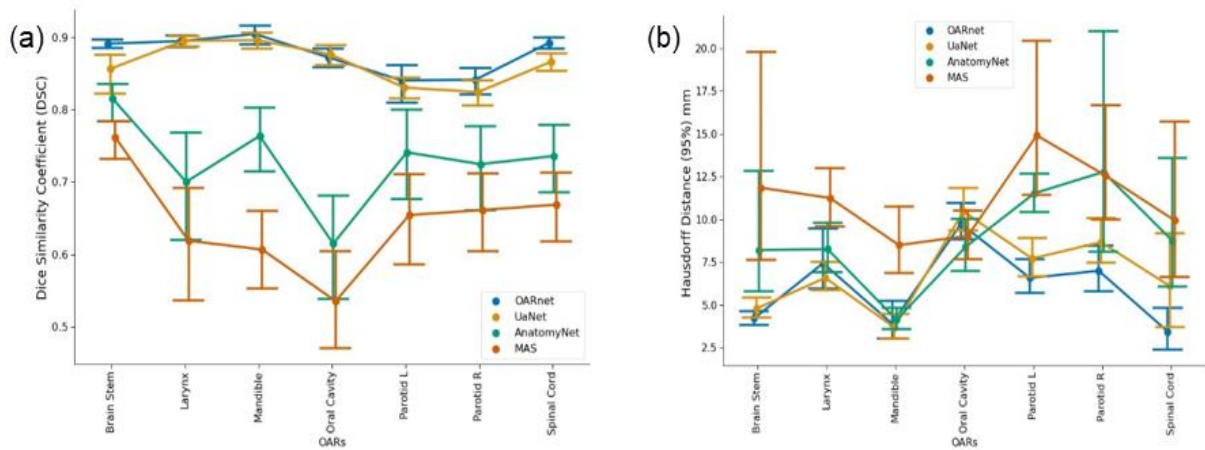


Figure 5 (a) Dice similarity coefficient and (b) Hausdorff comparison for the alternative delineation methods. The points in the graphs are mean values and bars show the 95% confidence intervals.

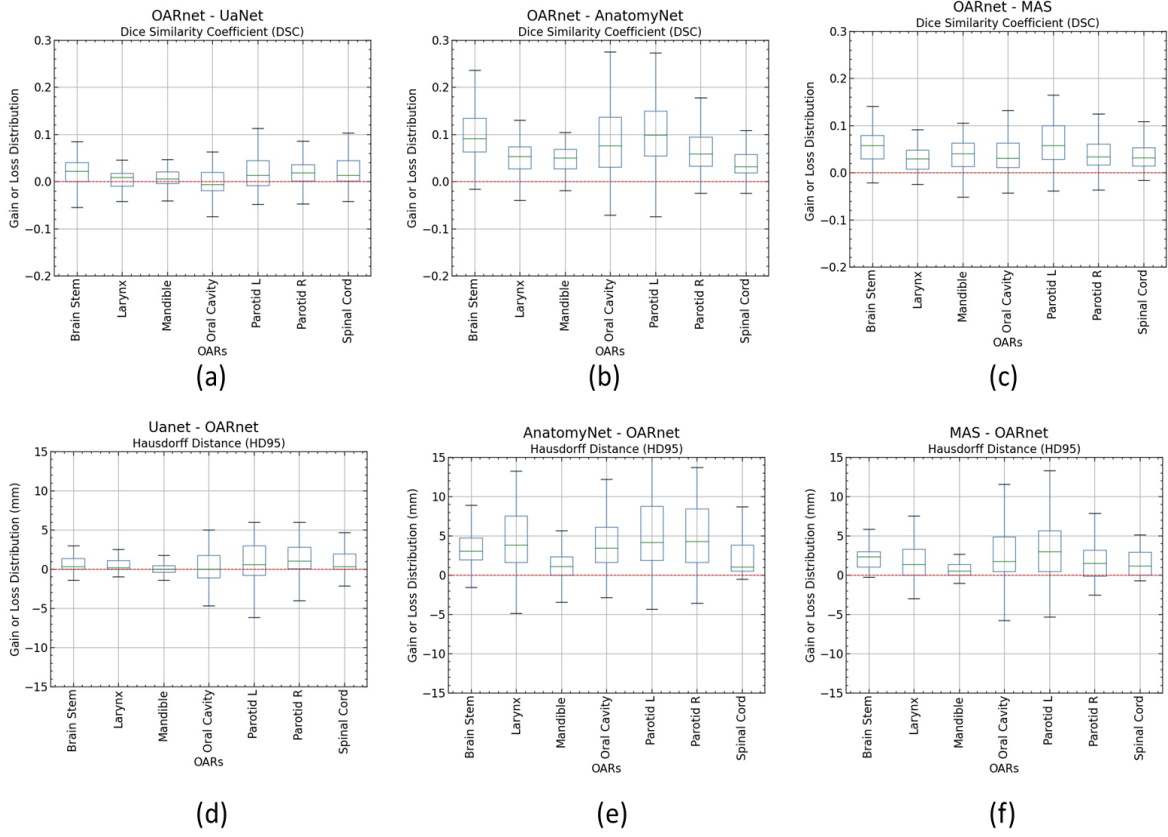


Figure 6 (a)-(c) Dice similarity coefficient gain or loss distributions of OARnet v/s UaNet, AnatomyNet, and MAS, respectively. (d)-(f) Hausdorff distance gain or loss distribution of OARnet v/s UaNet, AnatomyNet, and MAS, respectively. Dotted red line denotes no gain or loss.

Dosimetric inter-comparisons for the 56 dosimetric test patients are shown in Figure 7 and Figure 8, and Table 2 shows the gain or loss distribution for mean (*a,b,c*) and maximum (*d,e,f*) doses. Positive values indicate that OARnet is closer to the reference delineation results than the alternative. OARnet is closer to the reference delineation results than MAS and AnatomyNet, and is OARnet is equal or slightly closer than UaNet. The RSMEs [45] for each method are inter-compared in Figure 8. Results are mixed. In some cases, many cases OARnet and UaNet result in similar RMSE values with are lower than MAS and AnatomyNet, which are generally higher. However, the left parotid stands out with the OARnet being substantially higher than UaNet.

Figure 8 (c) and (d) show the mean absolute error for the mean and maximum doses with 95% confidence intervals (95 CI). One-sided Wilcoxon signed-rank test results for dose results are shown in Table 2. There are fewer OARs with statistically significant dosimetric improvements between OARnet and UaNet than geometric improvement, with 7/28 OARnet improvements for Dmax and 10/28 for Dmean. The opposite-sided Wilcoxon test finds that the UaNet improves Eye L mean dose prediction compared with OARnet. OARnet yields equivalent or better than UaNet maximum dose estimates for all OARs, and equivalent or better mean dose estimates for 27/28 OARs. AnatomyNet

and MAS also have fewer dosimetric than geometric differences but performed poorer than UaNet. OARnet yielded equivalent or better estimates of maximum and mean doses than both AnatomyNet and MAS for all OARs. Compared to UaNet, OARnet produced different dosimetric parotid results, but they were not statistically significant (Dmax p-value ~ 0.8 and Dmean \sim p-value ~ 0.65). UaNet and AnatomyNet are modeled based on 3D Unet architecture, while OARnet uses a DenseNet like network architecture. It is already proven the effectiveness of DenseNet over 3D Unet with less trainable parameters and training time[15], [16], [34].

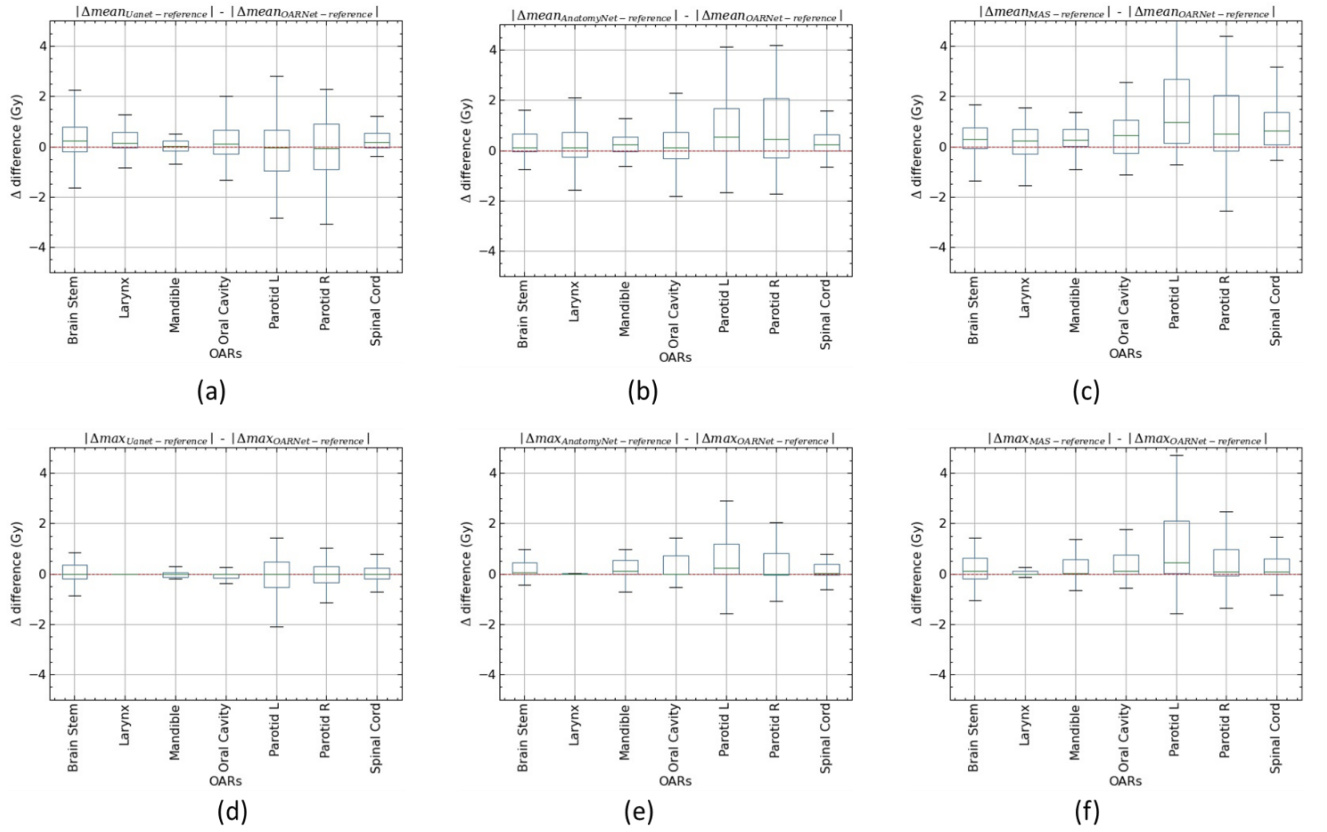


Figure 7 Dosimetric gain or loss for mean ((a), (b), and (c)) and maximum ((d),(e),(f)) doses comparing OARnet with the UaNet, AnatomyNet, and MAS with respect to the reference delineations.

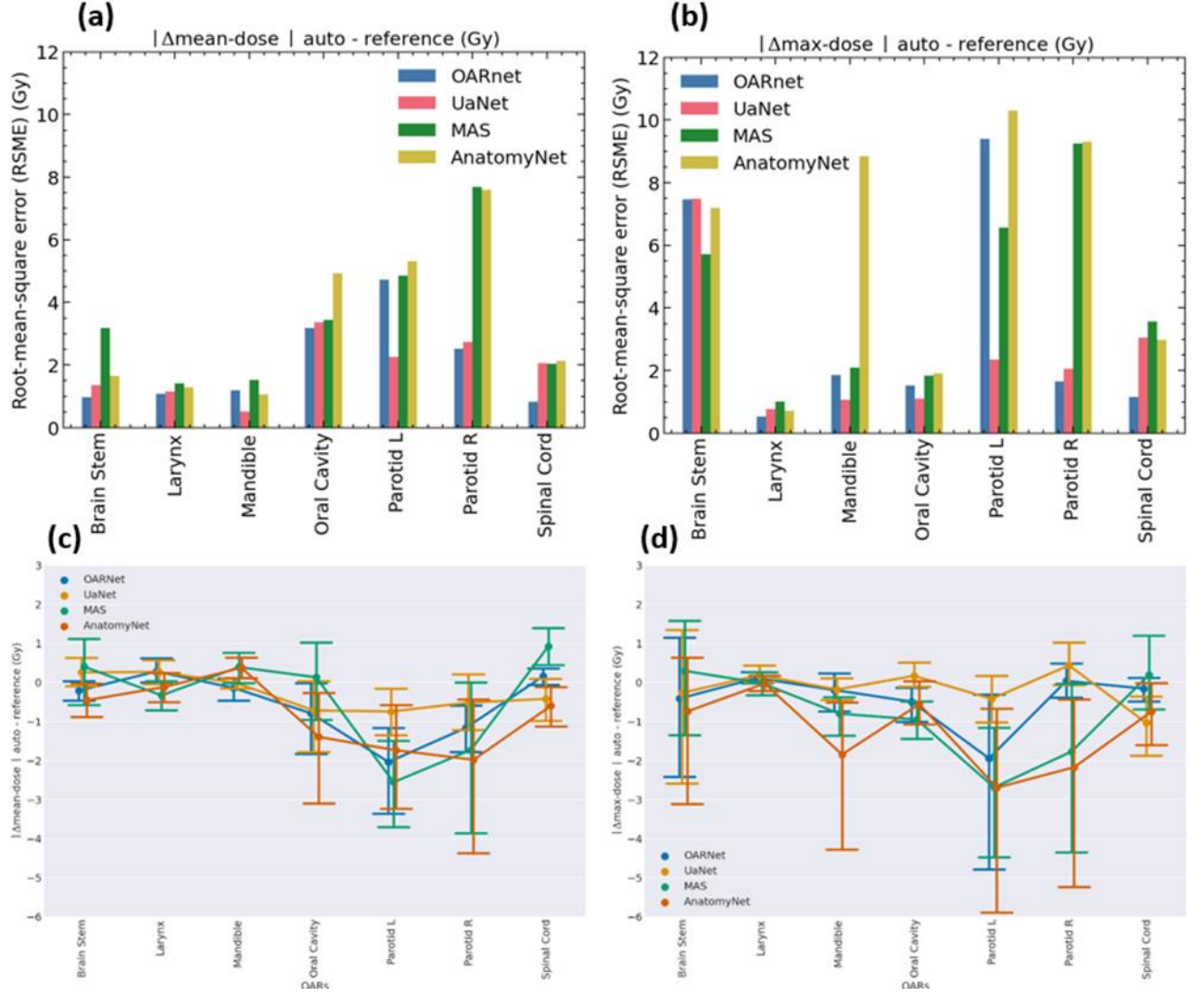


Figure 8 (a) Mean and (b) maximum doses between auto-delineation models and reference delineations using root-mean-square error (RSME). The dosimetric evaluation shows that OARnet produces smaller RSME for most structures. (c) and (d) compare mean and max doses between auto-delineation models and reference delineations using mean-absolute-error[46] (MAE) with confidence intervals (95 CI).

Table 2. One-sided Wilcoxon signed-rank test p -values comparing alternative methods with respect to OARnet on dosimetric metrics. The null hypothesis is that the results are the same distribution. Statistically significant results with p -value < 0.05 , marked with a *, indicate a preference for OARnet with smaller differences in Dmax and Dmean with respect to the reference delineations. The last two rows indicate the number of OARs in which OARnet or the alternative delineation method (UaNet, AnatomyNet, MAS) metric achieved statistical significance ($p < 0.05$). Per-OAR and per-delineation method results for the opposite-sided tests (e.g. UaNet-OARnet) are not shown due to the sparsity of the significant results.

* p -value < 0.05	ADmax - Wilcoxon signed rank test - OARnet less than other methods			ADmean - Wilcoxon signed rank test - OARnet less than other methods		
OARs	OARnet - UaNet (p -value)	OARnet - AnatomyNet (p -value)	OARnet - MAS (p -value)	OARnet - UaNet (p -value)	OARnet - AnatomyNet (p -value)	OARnet - MAS (p -value)
Brachial Plexus	0.63	*	*	0.39	0.91	*
Brain Stem	0.48	*	0.13	*	*	*
Pharyngeal Constrictor Muscle	0.92	*	0.27	0.75	*	*
Inner Ear L	*	0.25	0.63	*	*	0.31
Inner Ear R	*	0.28	0.31	*	*	0.51
Eye L	0.86	*	*	1.00	*	0.60
Eye R	0.08	*	*	0.56	*	*
Hypophysis	0.07	*	*	*	*	*
Larynx	0.13	0.13	*	*	0.07	0.08
Lens L	0.12	*	*	0.62	0.11	*
Lens R	0.47	*	*	0.08	*	*
Mandible	0.60	*	*	0.49	*	*
Optical Chiasm	*	*	*	0.70	*	0.12
Optical Nerve L	*	*	*	*	*	*
Optical Nerve R	0.15	0.06	*	0.22	*	*
Oral Cavity	0.36	0.06	*	0.24	0.38	*
Parotid L	0.78	*	*	0.64	*	*
Parotid R	0.80	*	*	0.65	*	*
SMG L	0.08	*	*	0.17	*	*
SMG R	0.20	0.12	0.08	0.24	*	*
Spinal Cord	0.21	*	*	*	*	*
Sublingual Gland	0.37	*	*	0.18	*	*
Temporal Lobe L	0.14	*	*	*	*	*
Temporal Lobe R	*	*	*	*	*	*
Thyroid	0.08	0.13	0.47	0.65	*	0.34
TMJ L	0.23	*	*	0.11	*	0.10
TMJ R	*	*	*	*	*	*
Trachea	*	*	*	0.35	*	*
N - OARnet - p -value < 0.05	7	21	22	10	24	21
N - other method - p -value < 0.05	0	0	0	1	0	0

4 Discussion

This research work introduced a compact deep learning-based method to automatically delineate OARs in H&N CT images. OARnet was intercompared with other machine-learning based delineation algorithms (UaNet [31], AnatomyNet [30]), as well as a MAS-based approach based on geometric and dosimetric metrics. OARnet delineation DSCs were statistically significant better than UaNet DSCs for 82% (23/28) of the delineations, and for 100% of the AnatomyNet and MAS delineations. The OARnet HD95s were statistically better than 61% of the UaNet delineations, and 96% of the AnatomyNet and MAS delineations.

UaNet and AnatomyNet are modeled based on 3D Unet architecture, while OARnet uses a DenseNet like network architecture. It is already proven the effectiveness of DenseNet over 3D Unet with less trainable parameters and training time [15], [16], [34]. Although OARnet was trained to delineating 28 specific H&N OARs, we see no technical reason why OARnet could not be trained to

delineate other OARs throughout the body, provided sufficient datasets existed for training and validation.

With data augmentation, the 235 datasets used for training, validating and testing the deep learning-based networks appeared to be adequate since the validation loss decreased with the decrement in training loss indicating no overfitting. Our number of datasets is less than that of other machine-learning based auto-delineation methods. Nonetheless, more datasets could tighten the gap between validation and training loss curves, and could potentially change the differential performance between e.g. OARnet and UaNet.

For manual delineations, the existence of inter- and intra-observer delineation variability is well known [3], [4], [47]–[49]. This implies that some delineation variability is clinically acceptable. Unfortunately, to the best of our knowledge, the acceptable level of variability cannot be reliably captured by DSC, HD95 or other geometric metrics. To accommodate this, some delineation studies have observers review resultant delineations for acceptability [5]–[7], [50], [51], and others have observers correct delineations, and measure the time to correct the delineations, or the geometric change in the delineation [52]–[57], [58]. While interesting, inclusion of these facets is outside the scope of this work, particularly considering the subjective nature of the acceptable/non-acceptable decision and inherent variability in delineation alterations.

Prior publications on UaNet [31], AnatomyNet [30] did not include any dosimetric evaluation. Here, to address acceptable variability, we have added a basic dosimetric evaluation in which dose metrics are evaluated with each method’s delineations for a plan developed based upon the reference manual delineations. The dosimetric advantage of OARnet compared with the other methods appears less compared to the geometric metrics. Dmax for OARnet was statistically closer to the reference delineation than UaNet for 25% of the delineations. UaNet Dmax was statistically closer to the reference than OARnet for 0 delineations. For Dmean, OARnet was statistically closer than UaNet for 36% of the delineations, but UaNet was statistically closer than OARnet for 1 delineation (Eye L). AnatomyNet and MAS uniformly performed poorer than UaNet for dosimetric endpoints.

Although we performed basic dosimetric analysis, in radiotherapy treatment planning, the delineations affect the shape of an optimized dose distribution. As such, full analysis of the acceptability of delineation variations or the potential clinical impact of alternative delineations can be accomplished by creating a treatment plan with each delineation, followed by evaluation with all other delineations [59]. Inclusion of these additional methods and analysis is beyond the scope of this work. Similarly, including the effect of other variations inherent to fractionated radiation therapy, such as daily setup variations [60], [51], can partly wash out the dosimetric differences between different delineations is beyond the scope.

Intercomparisons of Tables 1 and 2 yield some interesting observations. While for most instances in which *DSC* and *HD95* indicated no geometric advantage to OARnet, there was also no dosimetric advantage, there were exceptions. In comparison with UaNet, the OARnet Larynx *DSC* ($p=0.06$) and *HD95* ($p=0.09$) did not meet the $p<0.05$ significance threshold, however the mean dose difference did. For Temporal Lobe L, neither *DSC* ($p=0.06$) or *HD95* ($p=0.81$) reached significance, but both maximum and minimum doses did. Most interesting is Temporal Lobe R, in which the opposite-sided Wilcoxon test indicated statistical significance in that UaNet *HD95* was less than that for OARnet, but the dosimetric analysis indicated a statistically better mean and maximum dose differences for OARnet. These observations add to the evidence that geometric metrics might miss dosimetrically relevant differences.

As geometric and current dosimetric analysis are inadequate to prove absolute clinical suitability of OARnet (or any other) delineations, post-delineation human review, potential correction, and approval is still recommended for all auto-delineation methods. It has been shown the efficiency of the review process can be improved by prioritizing OARs into those which could potentially impact the dosimetric plan, hence require human review, and those which do not impact the dosimetric plan, hence do not require review [50]. To be clinically practical, such a prioritization process will be required for algorithms that delineate a large number of OARs as thorough manual review of e.g. all 28 H&N OARnet would challenge clinical resources. Compared with the current clinical standard of delineating 7-9 likely relevant H&N OARs, a benefit of combining a fully delineated dataset with a prioritization method is that OARs that are typically not delineated, but approach or exceed dose tolerances, are less likely to be missed. That is, auto-delineation combined with prioritization might reduce the risk of overdosing atypical OARs.

5 Conclusion

This work presents a compact method for auto-delineation of OARs using modern deep-learning methods. It uses DenseNet architecture but is optimized in a hybrid approach dividing the task into two steps: bounding box detection followed by learning features in a cropped space for each OAR. The performance of OARnet was intercompared with other auto-delineation methods for both geometric and dosimetric endpoints. OARnet was equal or better than UaNet for all but one geometric (Temporal Lobe L, *HD95*) and one dosimetric (Eye L, mean dose) endpoint. OARnet was better than or equal to MAS, and AnatomyNet for all geometric and dosimetric endpoints. High-quality auto-delineation algorithms like OARnet have the potential to improve radiation therapy automation while improving safety and efficiency.

6 Acknowledgments

This study is funded by NIH funding R01CA222216-01A1

The authors thank the creators of the public data sets: TCIA, University of California Irvine, DEEPVOXEL Inc, and PDDCA, A Public Domain Database for Computational Anatomy, for creating data sets used in this study.

References

- [1] X. Han *et al.*, “Atlas-Based Auto-segmentation of Head and Neck CT Images,” in *Medical Image Computing and Computer-Assisted Intervention -- MICCAI 2008*, 2008, pp. 434–441.
- [2] H. Vorwerk *et al.*, “Protection of quality and innovation in radiation oncology: The prospective multicenter trial the German Society of Radiation Oncology (DEGRO-QUIRO study): Evaluation of time, attendance of medical staff, and resources during radiotherapy with IMRT,” *Strahlentherapie und Onkol.*, vol. 190, no. 5, pp. 433–443, 2014, doi: 10.1007/s00066-014-0634-0.
- [3] X. Geets *et al.*, “Inter-observer variability in the delineation of pharyngo-laryngeal tumor, parotid glands and cervical spinal cord: Comparison between CT-scan and MRI,” *Radiother. Oncol.*, vol. 77, no. 1, pp. 25–31, 2005, doi: 10.1016/j.radonc.2005.04.010.
- [4] C. L. Brouwer *et al.*, “3D Variation in delineation of head and neck organs at risk,” *Radiat. Oncol.*, vol. 7, no. 1, p. 32, 2012, doi: 10.1186/1748-717X-7-32.
- [5] D. N. Teguh *et al.*, “Clinical validation of atlas-based auto-segmentation of multiple target volumes and normal tissue (swallowing/mastication) structures in the head and neck,” *Int. J. Radiat. Oncol. Biol. Phys.*, vol. 81, no. 4, pp. 950–957, 2011, doi: 10.1016/j.ijrobp.2010.07.009.
- [6] J. F. Daisne and A. Blumhofer, “Atlas-based automatic segmentation of head and neck organs at risk and nodal target volumes: A clinical validation,” *Radiat. Oncol.*, vol. 8, no. 1, pp. 1–11, 2013, doi: 10.1186/1748-717X-8-154.
- [7] A. K. Hoang Duc *et al.*, “Validation of clinical acceptability of an atlas-based segmentation algorithm for the delineation of organs at risk in head and neck cancer,” *Med. Phys.*, vol. 42, no. 9, pp. 5027–5034, 2015, doi: 10.1118/1.4927567.
- [8] H. Lee *et al.*, “Clinical evaluation of commercial atlas-based auto-segmentation in the head and neck region,” *Front. Oncol.*, vol. 9, no. APR, pp. 1–9, 2019, doi: 10.3389/fonc.2019.00239.
- [9] T. Rohlfing, R. Brandt, R. Menzel, D. B. Russakoff, and C. R. Maurer, “Quo Vadis, Atlas-Based Segmentation?,” in *Handbook of Biomedical Image Analysis: Volume III: Registration Models*, J. S. Suri, D. L. Wilson, and S. Laxminarayan, Eds. Boston, MA: Springer US, 2005,

pp. 435–486.

- [10] G. Sharp *et al.*, “Vision 20/20: Perspectives on automated image segmentation for radiotherapy,” *Med. Phys.*, vol. 41, no. 5, pp. 1–13, 2014, doi: 10.1118/1.4871620.
- [11] A. A. Qazi, V. Pekar, J. Kim, J. Xie, S. L. Breen, and D. A. Jaffray, “Auto-segmentation of normal and target structures in head and neck CT images: A feature-driven model-based approach,” *Med. Phys.*, vol. 38, no. 11, pp. 6160–6170, 2011, doi: 10.1118/1.3654160.
- [12] O. Ronneberger, P. Fischer, and T. Brox, “U-net: Convolutional networks for biomedical image segmentation,” *Lect. Notes Comput. Sci. (including Subser. Lect. Notes Artif. Intell. Lect. Notes Bioinformatics)*, vol. 9351, pp. 234–241, 2015, doi: 10.1007/978-3-319-24574-4_28.
- [13] Ö. Çiçek, A. Abdulkadir, S. S. Lienkamp, T. Brox, and O. Ronneberger, “3D U-net: Learning dense volumetric segmentation from sparse annotation,” *Lect. Notes Comput. Sci. (including Subser. Lect. Notes Artif. Intell. Lect. Notes Bioinformatics)*, vol. 9901 LNCS, pp. 424–432, 2016, doi: 10.1007/978-3-319-46723-8_49.
- [14] Q. Dou *et al.*, “3D deeply supervised network for automated segmentation of volumetric medical images,” *Med. Image Anal.*, vol. 41, pp. 40–54, 2017, doi: <https://doi.org/10.1016/j.media.2017.05.001>.
- [15] L. Yu *et al.*, “Automatic 3D Cardiovascular MR Segmentation with Densely-Connected Volumetric ConvNets,” in *Medical Image Computing and Computer-Assisted Intervention – MICCAI 2017*, 2017, pp. 287–295.
- [16] M. H. Soomro *et al.*, “Automated Segmentation of Colorectal Tumor in 3D MRI Using 3D Multiscale Densely Connected Convolutional Neural Network,” *J. Healthc. Eng.*, vol. 2019, p. 1075434, 2019, doi: 10.1155/2019/1075434.
- [17] X. Feng, K. Qing, N. J. Tustison, C. H. Meyer, and Q. Chen, “Deep convolutional neural network for segmentation of thoracic organs-at-risk using cropped 3D images,” *Med. Phys.*, vol. 46, no. 5, pp. 2169–2180, 2019, doi: 10.1002/mp.13466.
- [18] H. R. Roth *et al.*, “An application of cascaded 3D fully convolutional networks for medical image segmentation,” *Comput. Med. Imaging Graph.*, vol. 66, no. March, pp. 90–99, 2018, doi: 10.1016/j.compmedimag.2018.03.001.
- [19] D. J. Rhee *et al.*, “Automatic detection of contouring errors using convolutional neural networks,” *Med. Phys.*, vol. 46, no. 11, pp. 5086–5097, Nov. 2019, doi: 10.1002/mp.13814.
- [20] X. Ren *et al.*, “Interleaved 3D-CNNs for joint segmentation of small-volume structures in head and neck CT images,” *Med. Phys.*, vol. 45, no. 5, pp. 2063–2075, May 2018, doi: 10.1002/mp.12837.
- [21] K. Fritscher, P. Raudaschl, P. Zaffino, M. F. Spadea, G. C. Sharp, and R. Schubert, “Deep

Neural Networks for Fast Segmentation of 3D Medical Images BT - Medical Image Computing and Computer-Assisted Intervention – MICCAI 2016,” 2016, pp. 158–165.

- [22] B. Ibragimov and L. Xing, “Segmentation of organs-at-risks in head and neck CT images using convolutional neural networks,” no. October 2016, pp. 547–557, 2017, doi: 10.1002/mp.12045.
- [23] C. M. Tam, X. Yang, S. Tian, X. Jiang, J. J. Beitler, and S. Li, “Automated delineation of organs-at-risk in head and neck CT images using multi-output support vector regression,” in *Medical Imaging 2018: Biomedical Applications in Molecular, Structural, and Functional Imaging*, 2018, vol. 10578, pp. 502–511, doi: 10.1117/12.2292556.
- [24] X. Wu *et al.*, “Auto-contouring via Automatic Anatomy Recognition of Organs at Risk in Head and Neck Cancer on CT images,” *Proc. SPIE--the Int. Soc. Opt. Eng.*, vol. 10576, Feb. 2018, doi: 10.1117/12.2293946.
- [25] Y. Tong *et al.*, “Hierarchical model-based object localization for auto-contouring in head and neck radiation therapy planning,” *Proc. SPIE--the Int. Soc. Opt. Eng.*, vol. 10578, Feb. 2018, doi: 10.1117/12.2294042.
- [26] Z. Wang, L. Wei, L. Wang, Y. Gao, W. Chen, and D. Shen, “Hierarchical Vertex Regression-Based Segmentation of Head and Neck CT Images for Radiotherapy Planning,” *IEEE Trans. image Process. a Publ. IEEE Signal Process. Soc.*, vol. 27, no. 2, pp. 923–937, Feb. 2018, doi: 10.1109/TIP.2017.2768621.
- [27] C. E. Cardenas *et al.*, “Deep Learning Algorithm for Auto-Delineation of High-Risk Oropharyngeal Clinical Target Volumes With Built-In Dice Similarity Coefficient Parameter Optimization Function,” *Int. J. Radiat. Oncol. Biol. Phys.*, vol. 101, no. 2, pp. 468–478, Jun. 2018, doi: 10.1016/j.ijrobp.2018.01.114.
- [28] M. Schwier *et al.*, “Evaluation of deep learning methods for parotid gland segmentation from CT images Evaluation of deep learning methods for parotid gland segmentation from CT images,” vol. 6, no. 1, 2018, doi: 10.1117/1.JMI.6.1.011005.
- [29] S. Cros, E. Vorontsov, and S. Kadoury, “Managing Class Imbalance in Multi-Organ CT Segmentation in Head and Neck Cancer Patients,” in *2021 IEEE 18th International Symposium on Biomedical Imaging (ISBI)*, 2021, pp. 1360–1364, doi: 10.1109/ISBI48211.2021.9433991.
- [30] W. Zhu *et al.*, “AnatomyNet: Deep learning for fast and fully automated whole-volume segmentation of head and neck anatomy,” *Med. Phys.*, vol. 46, no. 2, pp. 576–589, 2019, doi: 10.1002/mp.13300.
- [31] H. Tang *et al.*, “Clinically applicable deep learning framework for organs at risk delineation in CT images,” *Nat. Mach. Intell.*, vol. 1, no. 10, pp. 480–491, 2019, doi: 10.1038/s42256-019-0099-z.

- [32] Y. Wang, L. Zhao, M. Wang, and Z. Song, "Organ at Risk Segmentation in Head and Neck CT Images Using a Two-Stage Segmentation Framework Based on 3D U-Net," *IEEE Access*, vol. 7, pp. 144591–144602, 2019, doi: 10.1109/ACCESS.2019.2944958.
- [33] H. Chen, Q. Dou, L. Yu, J. Qin, and P. A. Heng, "VoxResNet: Deep voxelwise residual networks for brain segmentation from 3D MR images," *Neuroimage*, vol. 170, no. April 2017, pp. 446–455, 2018, doi: 10.1016/j.neuroimage.2017.04.041.
- [34] G. Huang, Z. Liu, L. Van Der Maaten, and K. Q. Weinberger, "Densely Connected Convolutional Networks," in *2017 IEEE Conference on Computer Vision and Pattern Recognition (CVPR)*, 2017, pp. 2261–2269, doi: 10.1109/CVPR.2017.243.
- [35] K. He, X. Zhang, S. Ren, and J. Sun, "Deep residual learning for image recognition," *Proc. IEEE Comput. Soc. Conf. Comput. Vis. Pattern Recognit.*, vol. 2016-Decem, pp. 770–778, 2016, doi: 10.1109/CVPR.2016.90.
- [36] T. D. Bui, J. Shin, and T. Moon, "3D Densely Convolutional Networks for Volumetric Segmentation."
- [37] T. D. Bui, J. Shin, and T. Moon, "Skip-connected 3D DenseNet for volumetric infant brain MRI segmentation," *Biomed. Signal Process. Control*, vol. 54, p. 101613, 2019, doi: 10.1016/j.bspc.2019.101613.
- [38] J. A. Bosch, Walter R., Straube, William L., Matthews, John W., & Purdy, "Data From Head-Neck_Cetuximab," *Cancer Imaging Arch.*, 2015, doi: <http://doi.org/10.7937/K9/TCIA.2015.7AKGJUPZ>.
- [39] K. S. Martin Vallières, Emily Kay-Rivest, Léo Jean Perrin, Xavier Liem, Christophe Furstoss, Nader Khaouam, Phuc Félix Nguyen-Tan, Chang-Shu Wang, "Data from Head-Neck-PET-CT," *Cancer Imaging Arch.*, 2017, doi: 10.7937/K9/TCIA.2017.8oje5q00.
- [40] R. Girshick, "Fast R-CNN," *Proc. IEEE Int. Conf. Comput. Vis.*, vol. 2015 Inter, pp. 1440–1448, 2015, doi: 10.1109/ICCV.2015.169.
- [41] D. P. Kingma and J. L. Ba, "Adam: A method for stochastic optimization," *3rd Int. Conf. Learn. Represent. ICLR 2015 - Conf. Track Proc.*, pp. 1–15, 2015.
- [42] L. R. Dice, "Measures of the Amount of Ecologic Association Between Species Author (s): Lee R . Dice Published by: Ecological Society of America Stable URL : <http://www.jstor.org/stable/1932409>," *Ecology*, vol. 26, no. 3, pp. 297–302, 1945.
- [43] A. A. Taha and A. Hanbury, "Metrics for evaluating 3D medical image segmentation: Analysis, selection, and tool," *BMC Med. Imaging*, vol. 15, no. 1, 2015, doi: 10.1186/s12880-015-0068-x.
- [44] L. V van Dijk *et al.*, "Improving automatic delineation for head and neck organs at risk by Deep

- Learning Contouring,” *Radiother. Oncol.*, vol. 142, pp. 115–123, 2020, doi: <https://doi.org/10.1016/j.radonc.2019.09.022>.
- [45] “Root-mean-square deviation - Wikipedia.” .
- [46] “Mean absolute error - Wikipedia.” .
- [47] J. van der Veen, A. Gulyban, S. Willems, F. Maes, and S. Nuyts, “Interobserver variability in organ at risk delineation in head and neck cancer,” *Radiat. Oncol.*, vol. 16, no. 1, p. 120, 2021, doi: 10.1186/s13014-020-01677-2.
- [48] S. K. Vinod, M. G. Jameson, M. Min, and L. C. Holloway, “Uncertainties in volume delineation in radiation oncology: A systematic review and recommendations for future studies,” *Radiother. Oncol.*, vol. 121, no. 2, pp. 169–179, 2016, doi: <https://doi.org/10.1016/j.radonc.2016.09.009>.
- [49] M. Machiels *et al.*, “Reduced inter-observer and intra-observer delineation variation in esophageal cancer radiotherapy by use of fiducial markers,” *Acta Oncol. (Madr)*, vol. 58, no. 6, pp. 943–950, Jun. 2019, doi: 10.1080/0284186X.2019.1588991.
- [50] E. Aliotta, H. Nourzadeh, W. Choi, V. G. Leandro Alves, and J. V Siebers, “An Automated Workflow to Improve Efficiency in Radiation Therapy Treatment Planning by Prioritizing Organs at Risk,” *Adv. Radiat. Oncol.*, vol. 5, no. 6, pp. 1324–1333, 2020, doi: 10.1016/j.adro.2020.06.012.
- [51] E. Aliotta, H. Nourzadeh, and J. Siebers, “Quantifying the dosimetric impact of organ-at-risk delineation variability in head and neck radiation therapy in the context of patient setup uncertainty,” *Phys. Med. Biol.*, vol. 64, no. 13, p. 135020, Jul. 2019, doi: 10.1088/1361-6560/ab205c.
- [52] C. E. Cardenas, J. Yang, B. M. Anderson, L. E. Court, and K. B. Brock, “Advances in Auto-Segmentation,” *Semin. Radiat. Oncol.*, vol. 29, no. 3, pp. 185–197, Jul. 2019, doi: 10.1016/j.semradonc.2019.02.001.
- [53] M. Kosmin *et al.*, “Rapid advances in auto-segmentation of organs at risk and target volumes in head and neck cancer,” *Radiother. Oncol. J. Eur. Soc. Ther. Radiol. Oncol.*, vol. 135, pp. 130–140, Jun. 2019, doi: 10.1016/j.radonc.2019.03.004.
- [54] T. Lustberg *et al.*, “Clinical evaluation of atlas and deep learning based automatic contouring for lung cancer,” *Radiother. Oncol. J. Eur. Soc. Ther. Radiol. Oncol.*, vol. 126, no. 2, pp. 312–317, Feb. 2018, doi: 10.1016/j.radonc.2017.11.012.
- [55] J. van der Veen *et al.*, “Benefits of deep learning for delineation of organs at risk in head and neck cancer,” *Radiother. Oncol. J. Eur. Soc. Ther. Radiol. Oncol.*, vol. 138, pp. 68–74, Sep. 2019, doi: 10.1016/j.radonc.2019.05.010.
- [56] L. Vandewinckele *et al.*, “Overview of artificial intelligence-based applications in radiotherapy:

- Recommendations for implementation and quality assurance,” *Radiother. Oncol.*, vol. 153, pp. 55–66, 2020, doi: <https://doi.org/10.1016/j.radonc.2020.09.008>.
- [57] K. J. Kiser, A. Barman, S. Stieb, C. D. Fuller, and L. Giancardo, “Novel Autosegmentation Spatial Similarity Metrics Capture the Time Required to Correct Segmentations Better Than Traditional Metrics in a Thoracic Cavity Segmentation Workflow,” *J. Digit. Imaging*, vol. 34, no. 3, pp. 541–553, Jun. 2021, doi: 10.1007/s10278-021-00460-3.
- [58] C. L. Brouwer *et al.*, “Assessment of manual adjustment performed in clinical practice following deep learning contouring for head and neck organs at risk in radiotherapy,” *Phys. Imaging Radiat. Oncol.*, vol. 16, pp. 54–60, 2020, doi: <https://doi.org/10.1016/j.phro.2020.10.001>.
- [59] “Comprehensive analysis and mitigation of the clinical effects of delineation and geometric uncertainties in conformal radiation therapy - Jeffrey Siebers.”.
- [60] H. Nourzadeh, W. T. Watkins, M. Ahmed, C. Hui, D. Schlesinger, and J. V. Siebers, “Clinical adequacy assessment of autocontours for prostate IMRT with meaningful endpoints;,” *Med. Phys.*, vol. 44, no. 4, pp. 1525–1537, 2017, doi: 10.1002/mp.12158.

1. OARnet Architecture:

Table 3 OARnet network configuration for delineating OARs

Layer	Kernel size	Output
Conv3D-BN-ReLU	$3 \times 3 \times 3, s = 1, p = 1$	$16 \times 128 \times 128 \times 128$
Conv3D	$3 \times 3 \times 3, s = 2, p = 1$	$16 \times 64 \times 64 \times 64$
Dense block 1 (k=16)	$\begin{bmatrix} 1 \times 1 \times 1, s = 1, p = 1 \\ 3 \times 3 \times 3, s = 1, p = 1 \end{bmatrix}_{\times 2}$	$48 \times 64 \times 64 \times 64$
Maxpool3D	$2 \times 2 \times 2, s = 2, p = 0$	$48 \times 32 \times 32 \times 32$
Dense block 2 (k=16)	$\begin{bmatrix} 1 \times 1 \times 1, s = 1, p = 1 \\ 3 \times 3 \times 3, s = 1, p = 1 \end{bmatrix}_{\times 2}$	$80 \times 32 \times 32 \times 32$
Maxpool3D	$2 \times 2 \times 2, s = 2, p = 0$	$80 \times 16 \times 16 \times 16$
Dense block 3 (k=16)	$\begin{bmatrix} 1 \times 1 \times 1, s = 1, p = 1 \\ 3 \times 3 \times 3, s = 1, p = 1 \end{bmatrix}_{\times 2}$	$112 \times 16 \times 16 \times 16$
Upsampling3D_1	$4 \times 4 \times 4, s = 2, p = 1, m = 12$	$16 \times 128 \times 128 \times 128$
Upsampling3D_2	$4 \times 4 \times 4, s = 4, p = 1, m = 12$	$16 \times 128 \times 128 \times 128$
Upsampling3D_3	$4 \times 4 \times 4, s = 8, p = 1, m = 12$	$16 \times 128 \times 128 \times 128$
Concatenation-BN-ReLU	--	$64 \times 128 \times 128 \times 128$
Classification	$1 \times 1 \times 1, s = 1, p = 1$	$29 \times 128 \times 128 \times 128$
Output shape=(channel×depth×height×width), s, p, k, m represent stride, padding, growth rate, and group respectively.		

The proposed network architecture is presented in Table 1. The network is consisted of contracting and expending paths. The contracting path aims to increase the receptive fields of feature maps. Three

dense blocks were used to extract features. Each dense block was comprised of two $3 \times 3 \times 3$ Conv-BN-ReLU. To overcome the overfitting, the dropout layer with a dropout rate of 0.2 is used after each dense block. The transition block that comprises a convolutional layer with the kernel size of $1 \times 1 \times 1$ followed by a pooling layer of $2 \times 2 \times 2$ with stride = 2 to increase the receptive field by down-sampling the input resolution. The expanding path aims to recover input resolution by 3D-Upsampling operators. To capture multiple levels of contextual information, the up-sampled feature maps from dense blocks are concatenated. In the last layer, we used $1 \times 1 \times 1$ convolution to classify each pixel to one of the 29 class outputs using the concatenated feature maps.

2. Geometric Analysis for 28 OARs

2.1 Dice Similarity Coefficient (DSC)

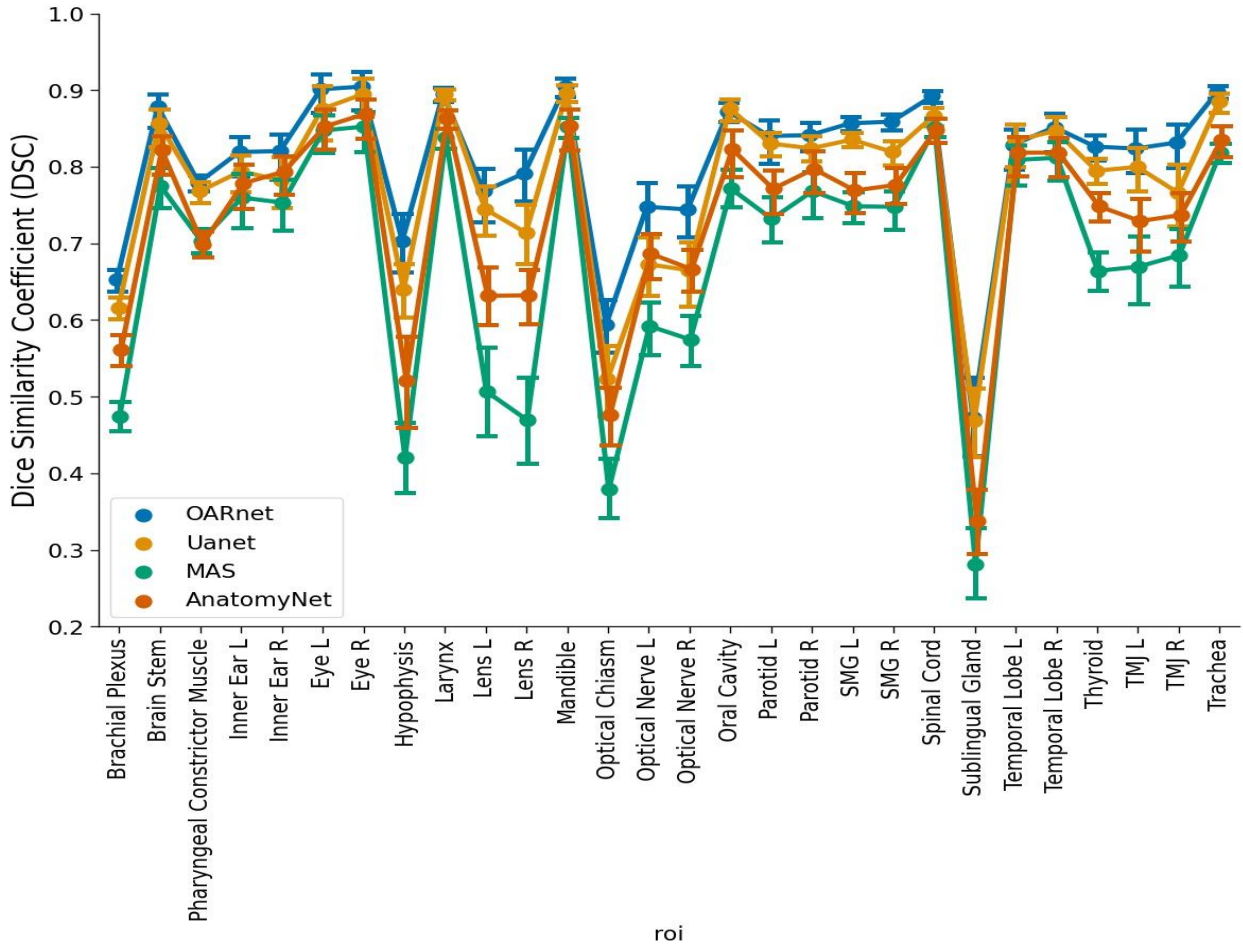


Figure 9 Dice similarity coefficient comparison between OARnet and alternative delineation methods for 28 OARs.

2.2 Hausdorff Distance

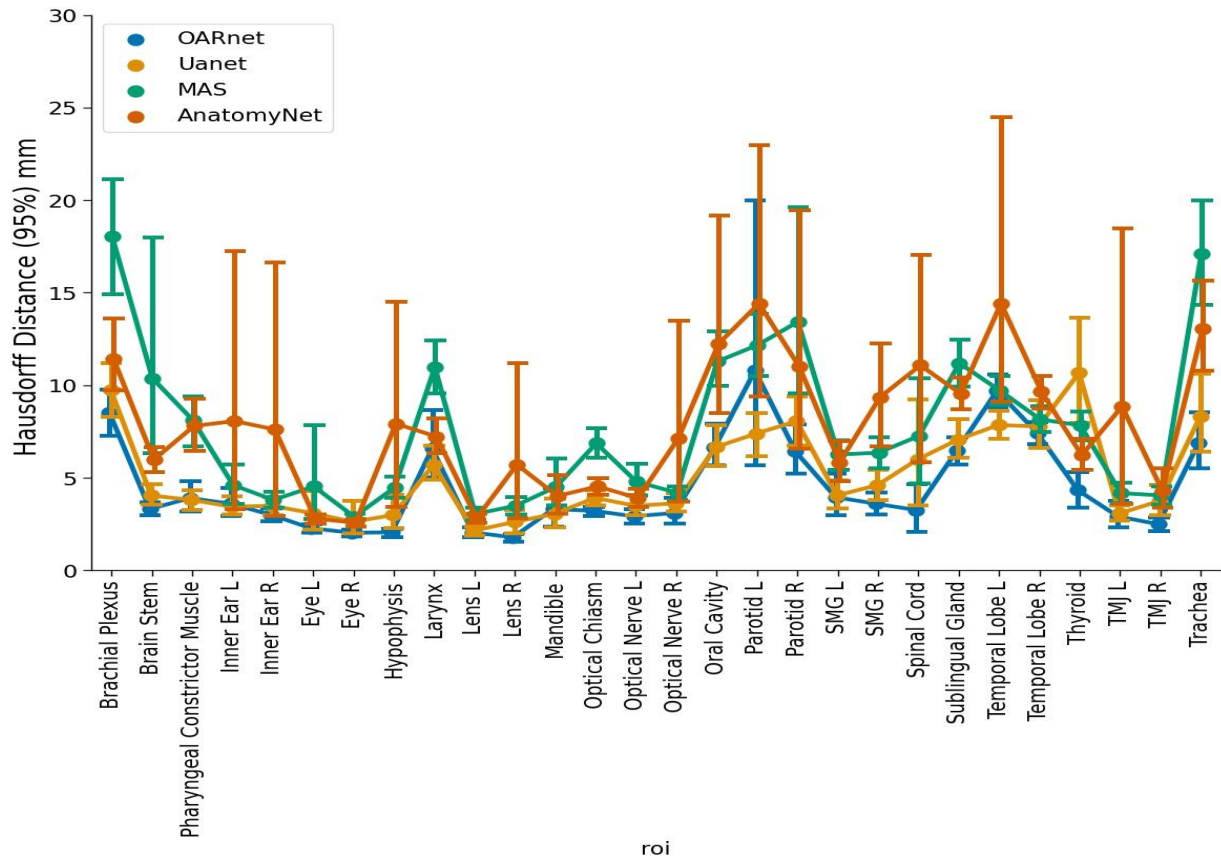


Figure 10 Hausdorff distance comparison between OARnet and alternative delineation methods for 28 OARs

2.3 Gain or Loss (GoL) for DSC

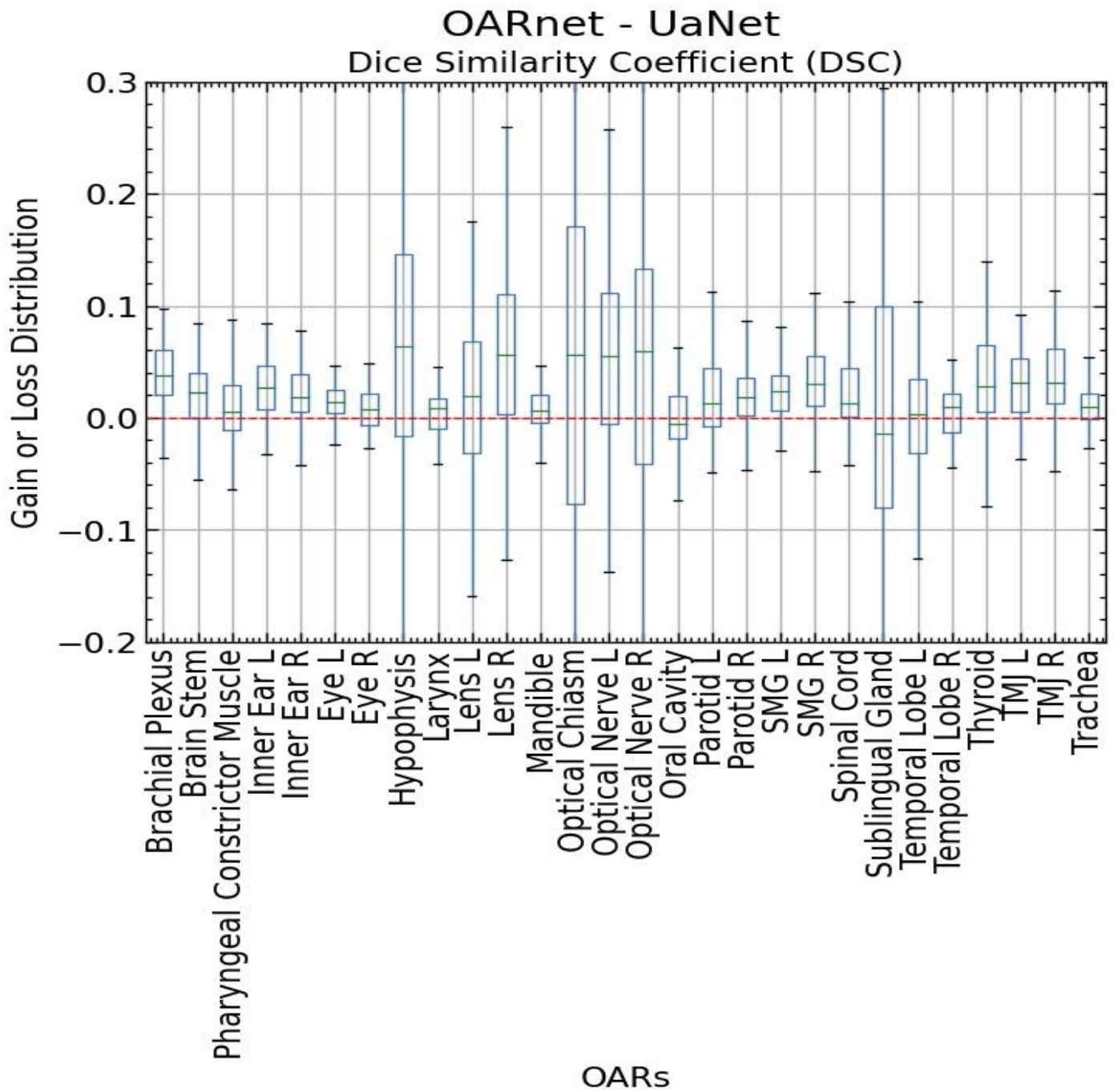


Figure 11 DSC gain or loss distribution of OARnet v/s UaNet for 28 OARs

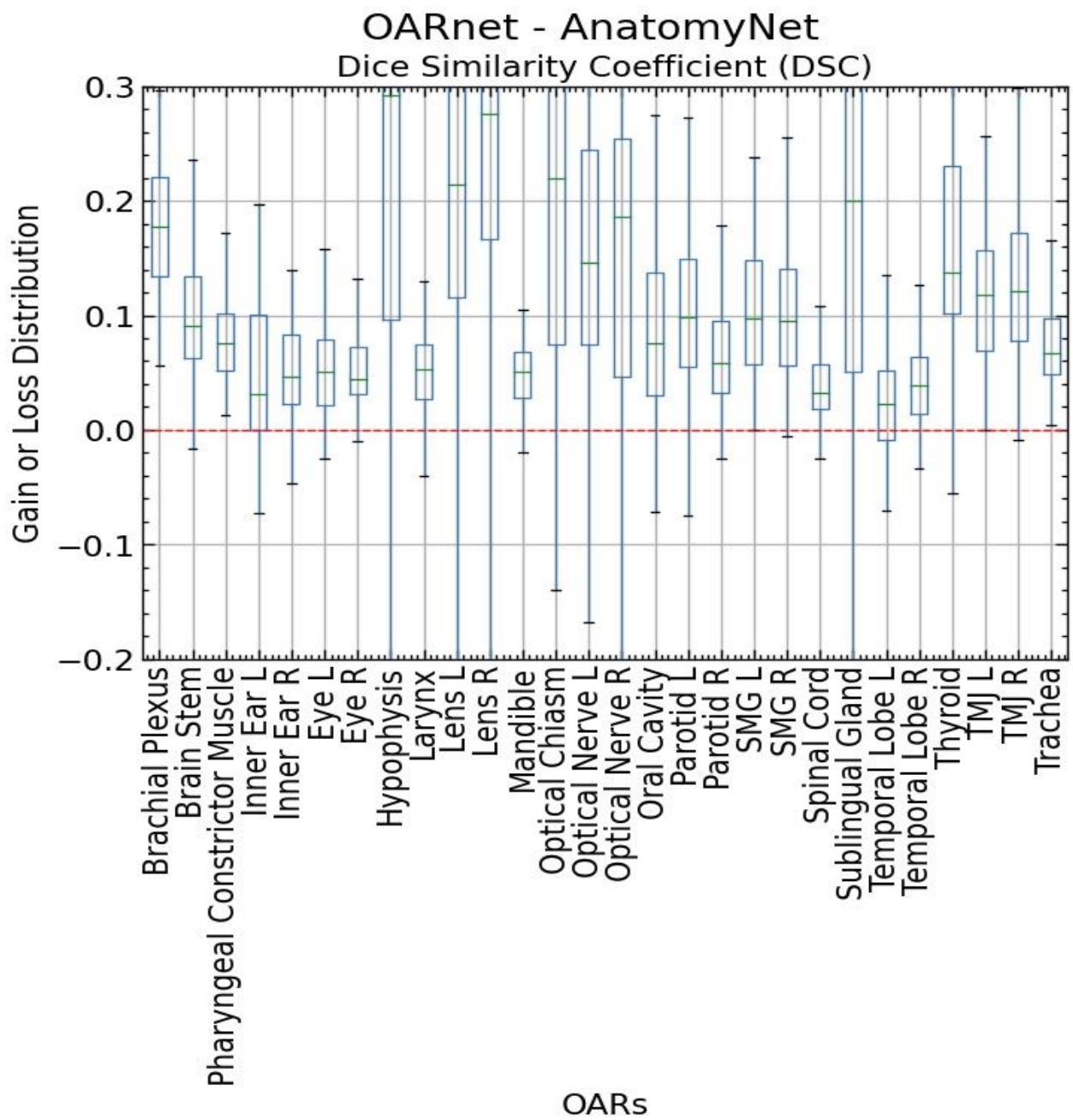


Figure 12 DSC gain or loss distribution of OARnet v/s AnatomyNet for 28 OARs

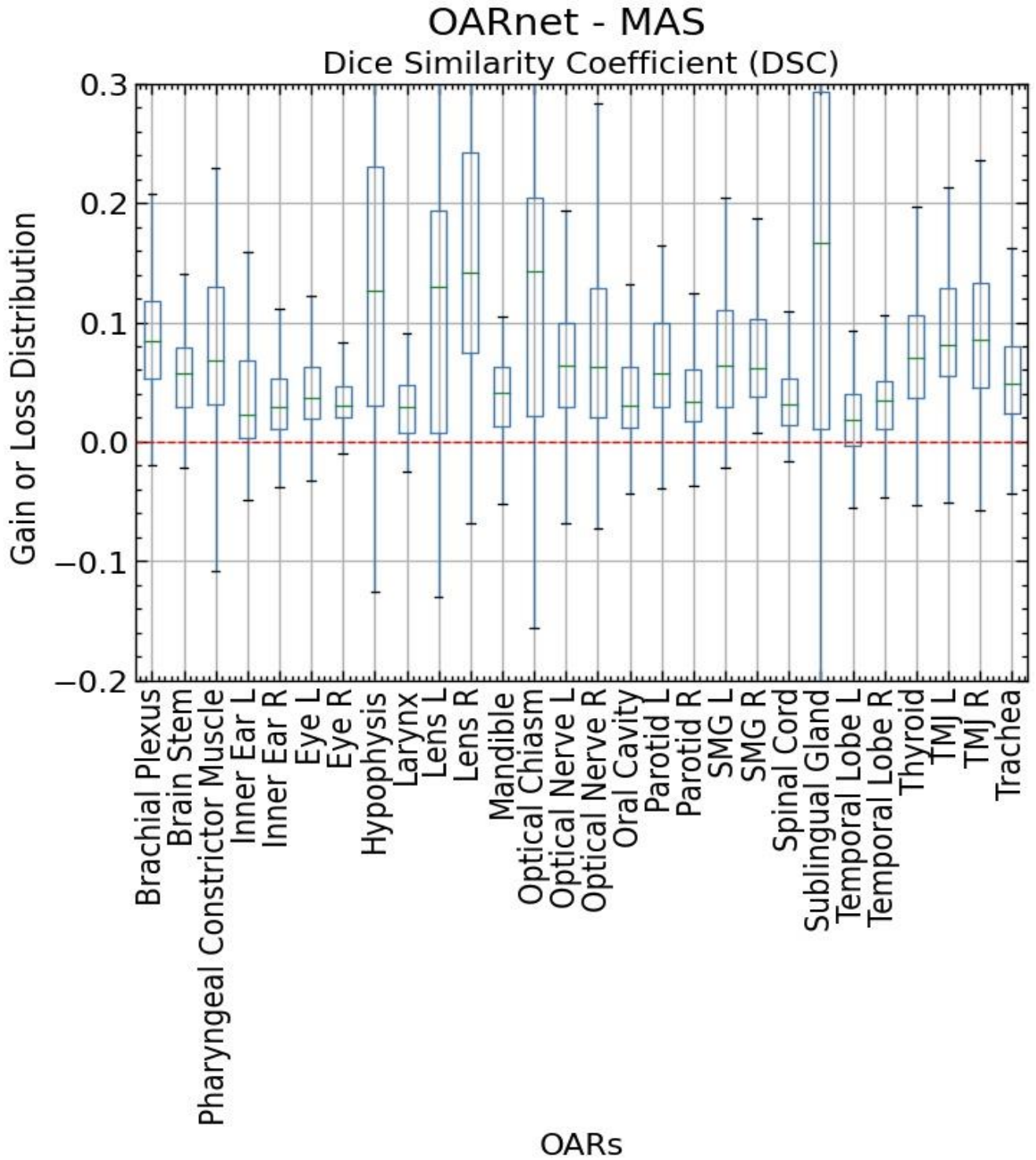


Figure 13 DSC gain or loss distribution of OARnet v/s MAS for 28 OARs

2.4 Gain or Loss (GoL) for HD95

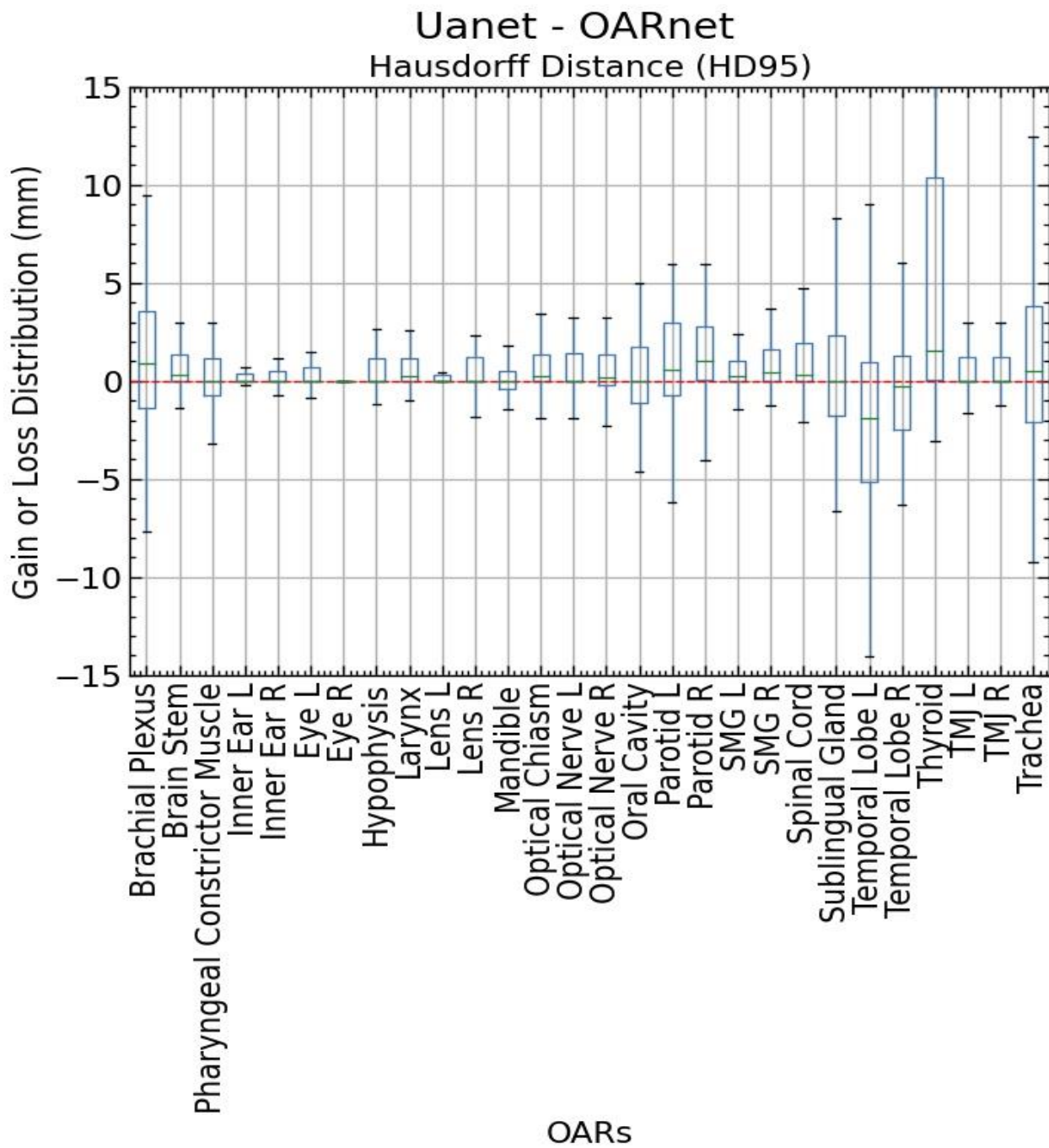


Figure 14 HD95 gain or loss distribution of OARnet v/s UaNet for 28 OARs

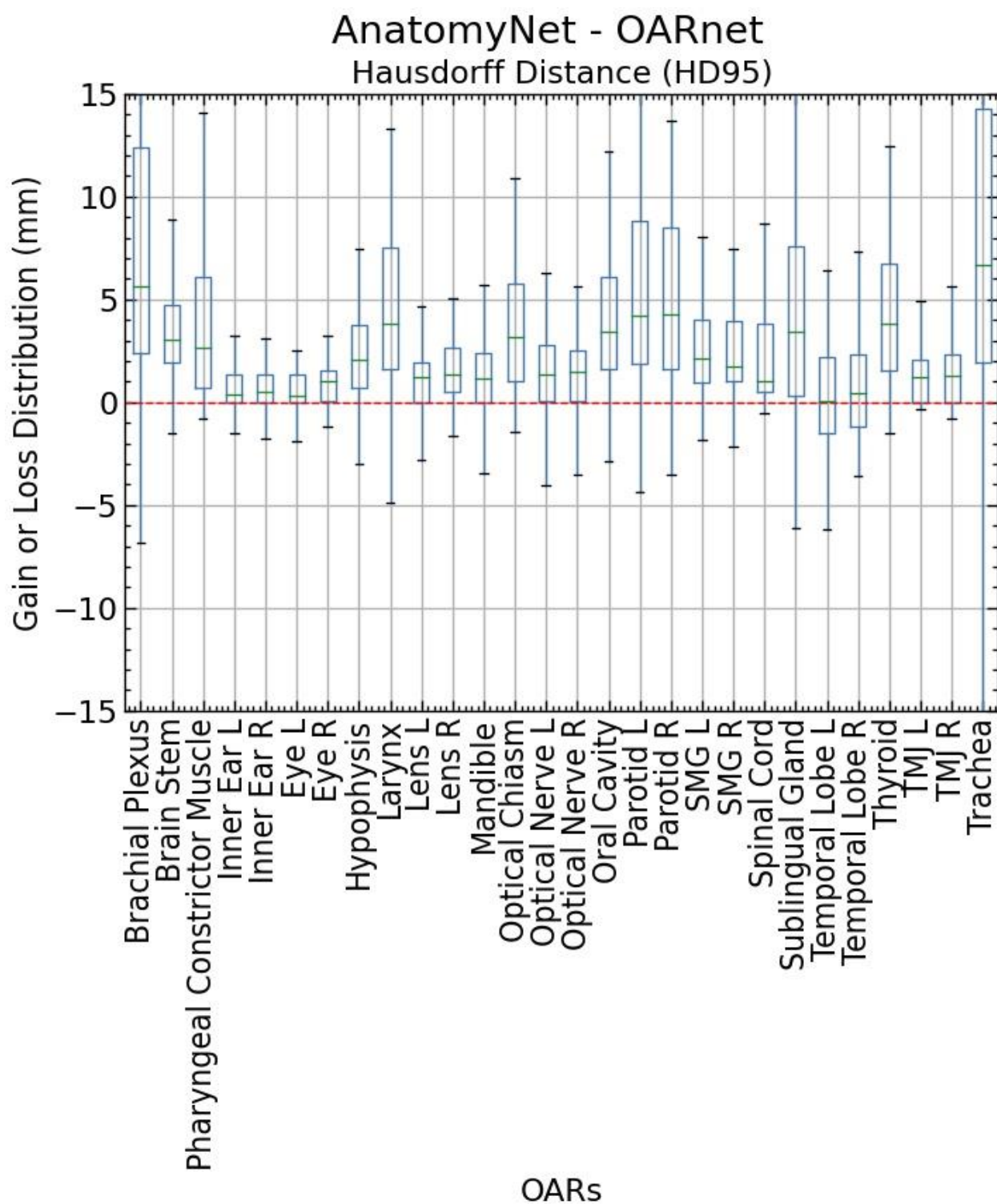


Figure 15 HD95 gain or loss distribution of OARnet v/s AnatomyNet for 28 OARs

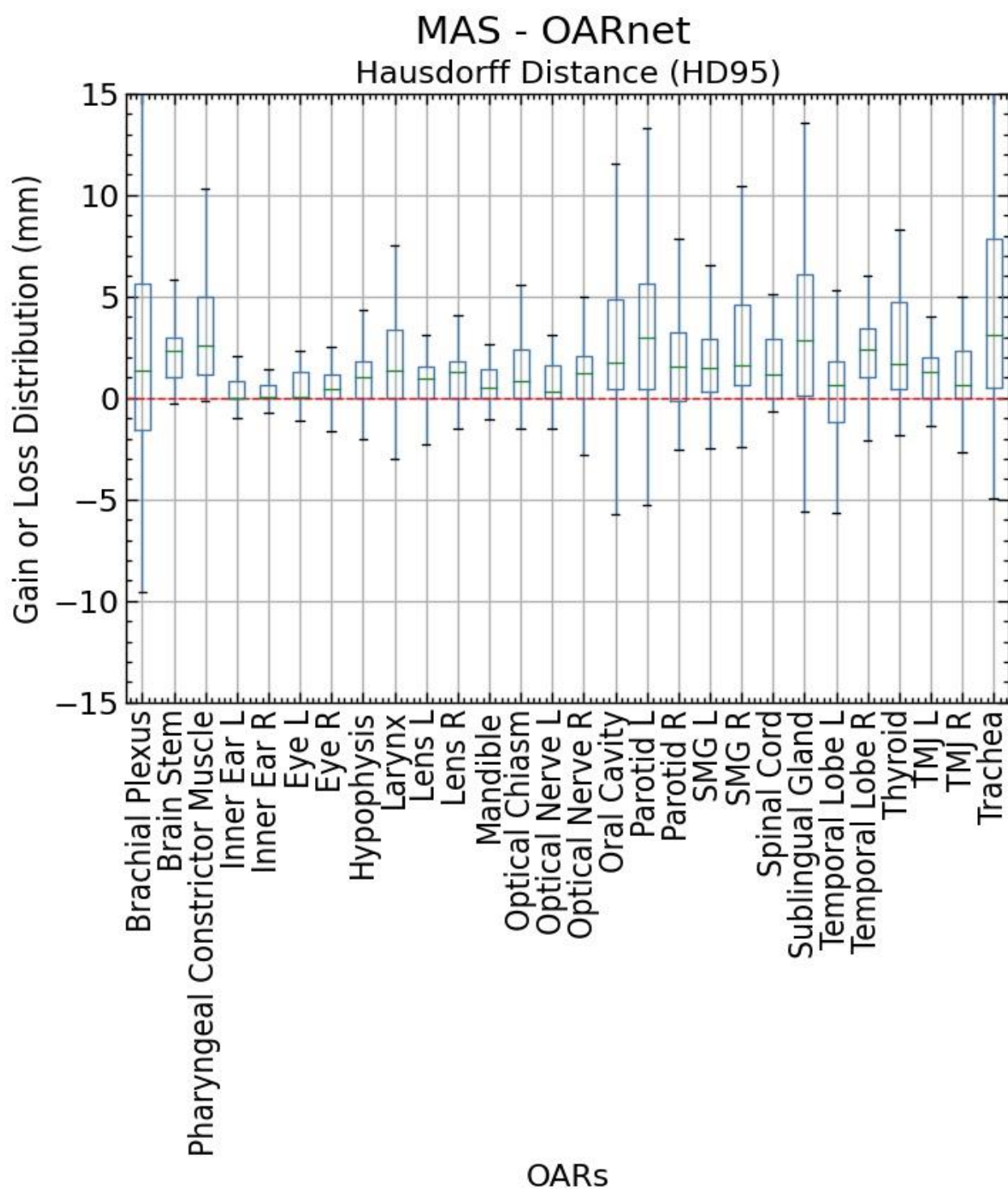


Figure 16 HD95 gain or loss distribution of OARnet v/s MAS for 28 OARs

3. Dosimetric Analysis for 28 OARs

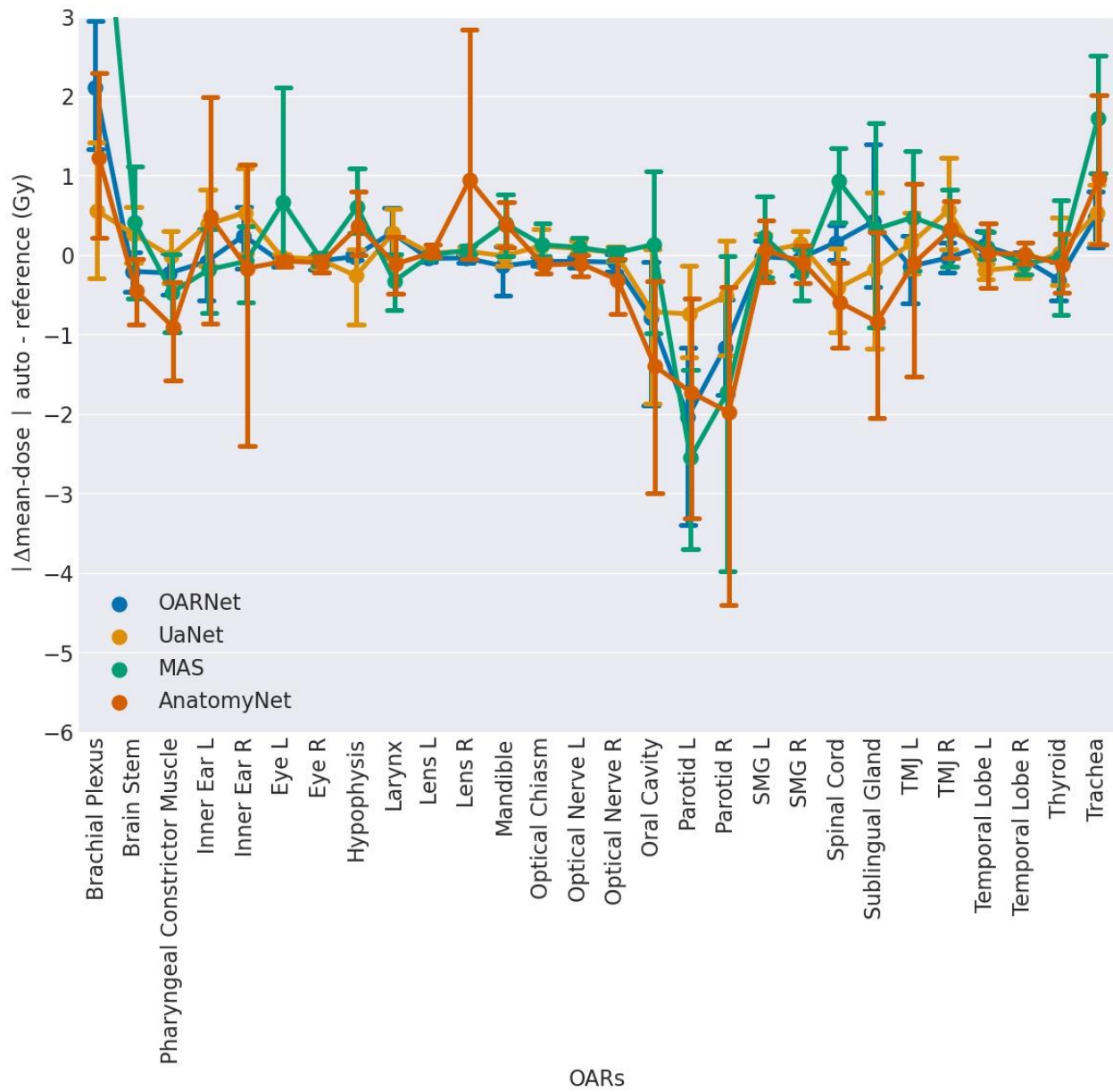


Figure 17 Mean doses between auto-delineation methods and reference contours using mean-absolute-error (MAE) for 28 OARs

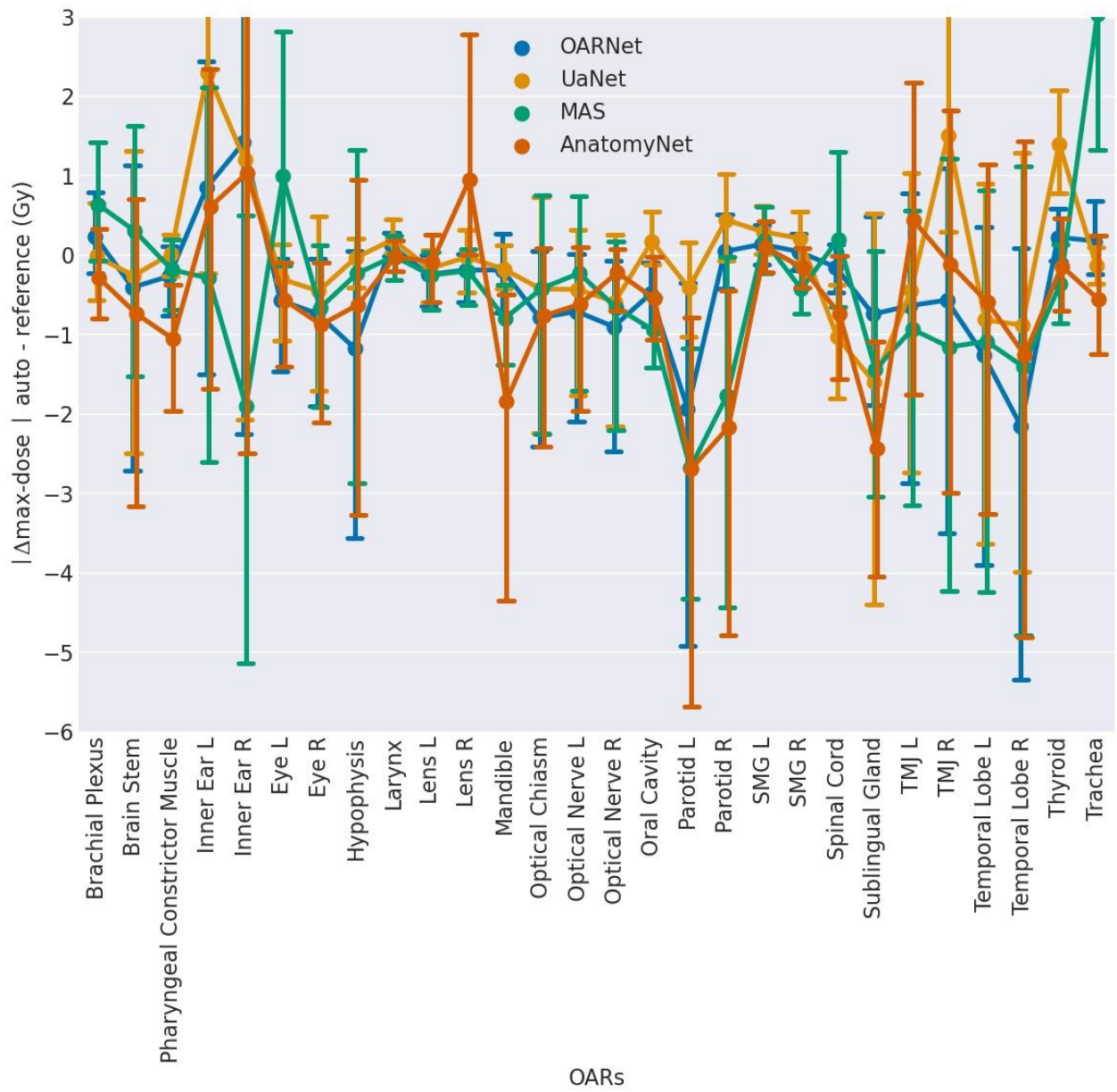


Figure 18 Max doses between auto-delineation methods and reference contours using mean-absolute-error (MAE) for 28 OARs

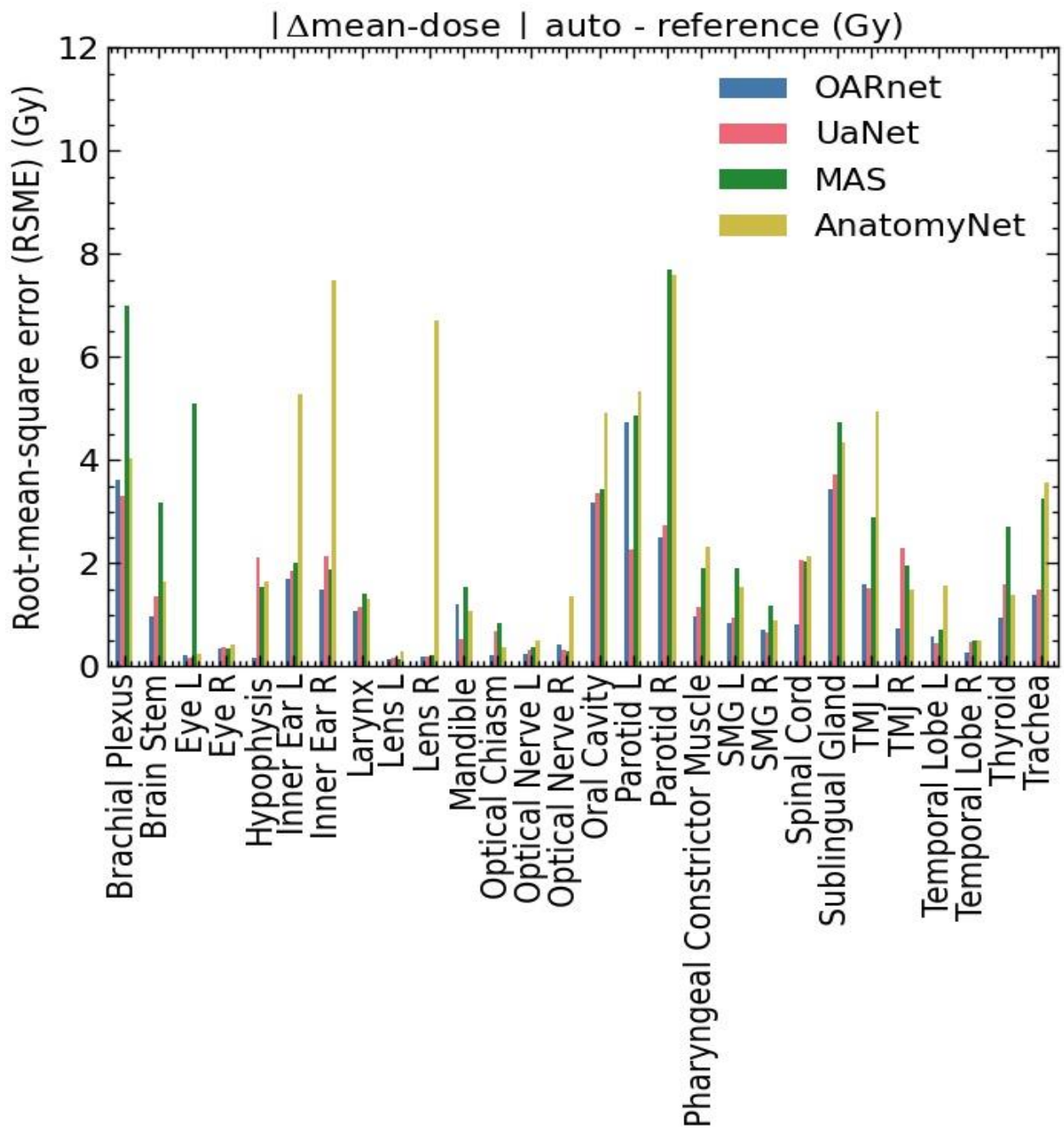


Figure 19 Mean doses between auto-delineation methods and reference contours using root-mean-square error (RSME) for 28 OARs.

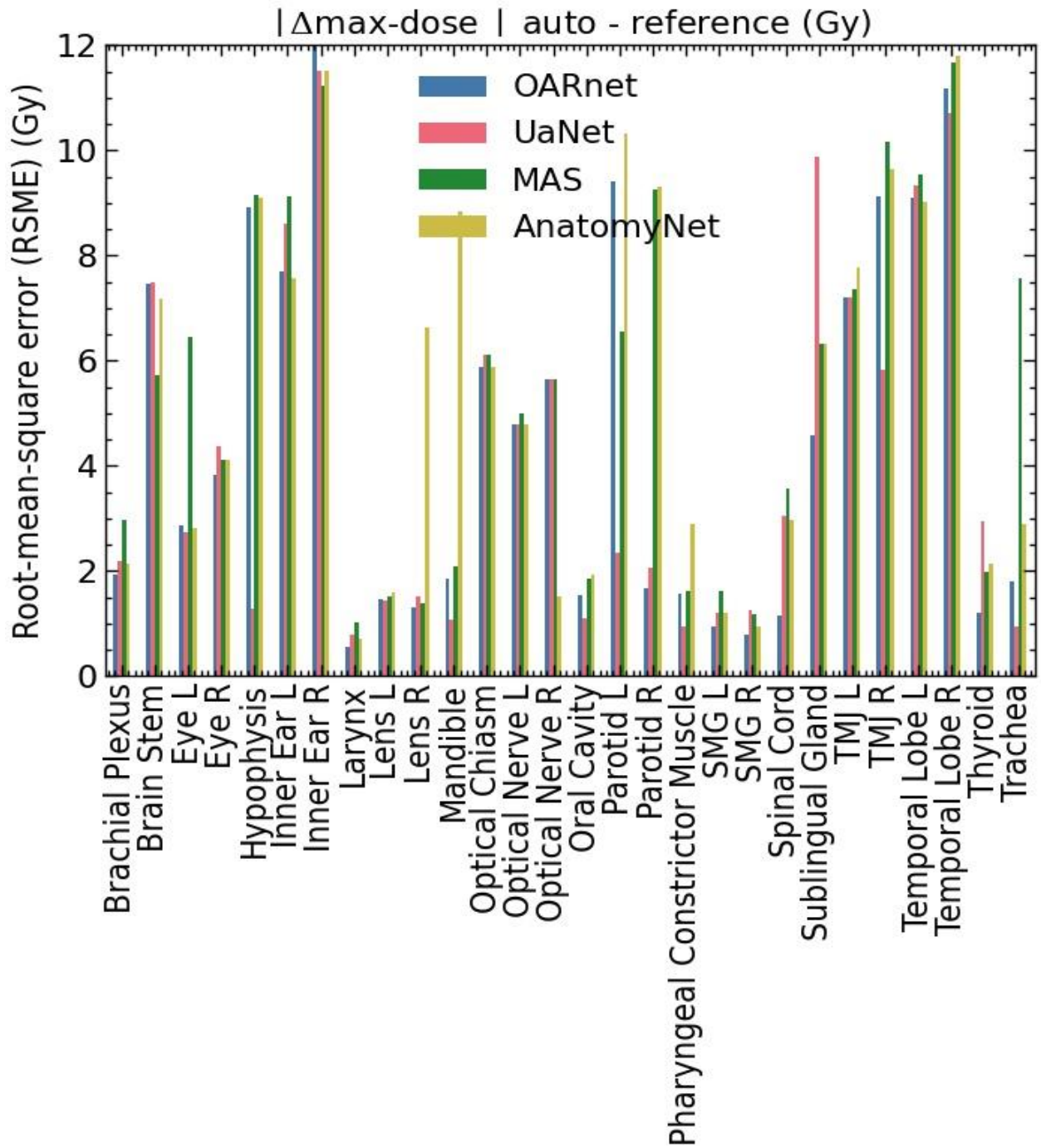


Figure 20 Max doses between auto-delineation methods and reference contours using root-mean-square error (RSME) for 28 OARs.

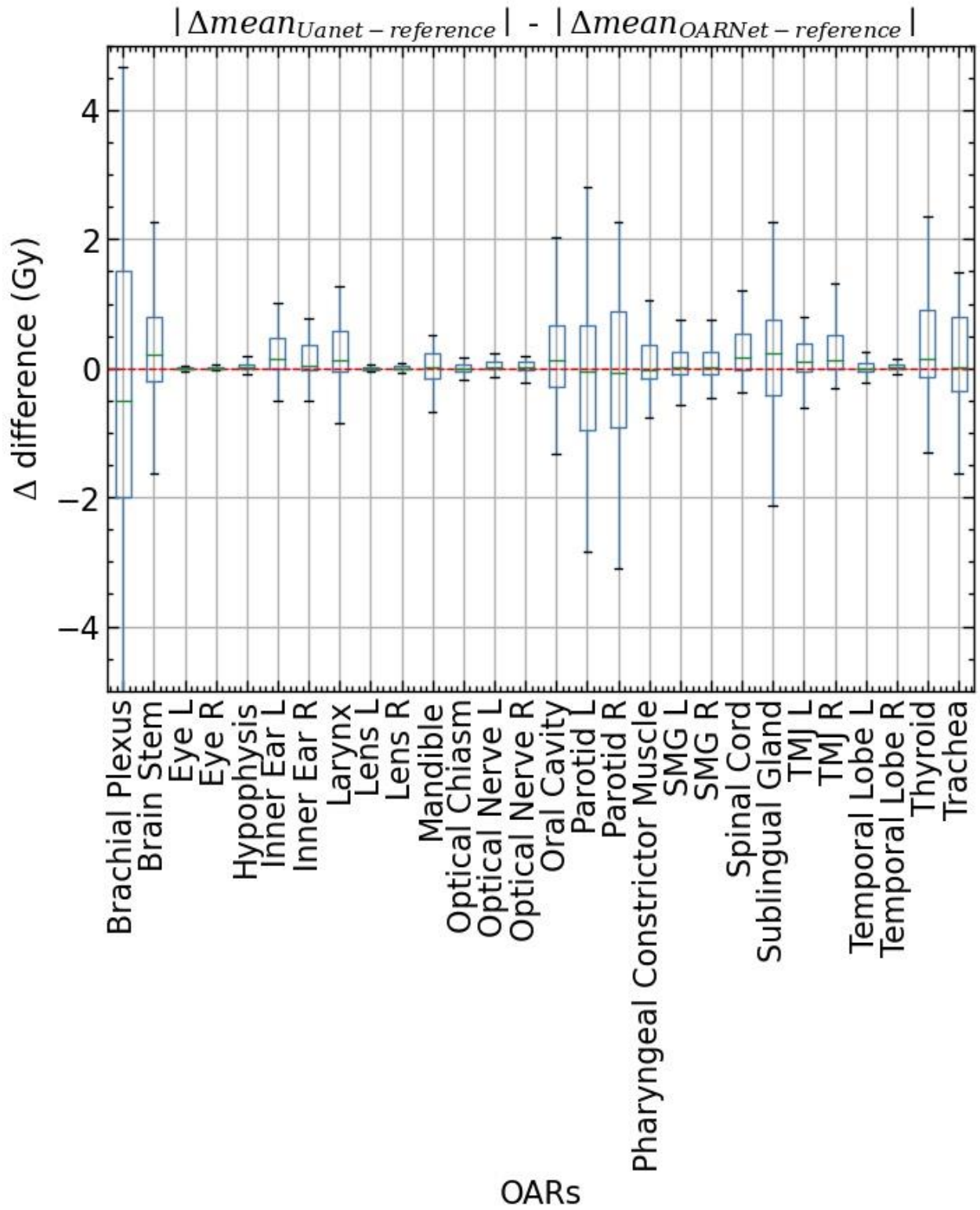


Figure 21 Dosimetric gain or loss for mean doses comparing OARnet with the UaNet for 28 OARs

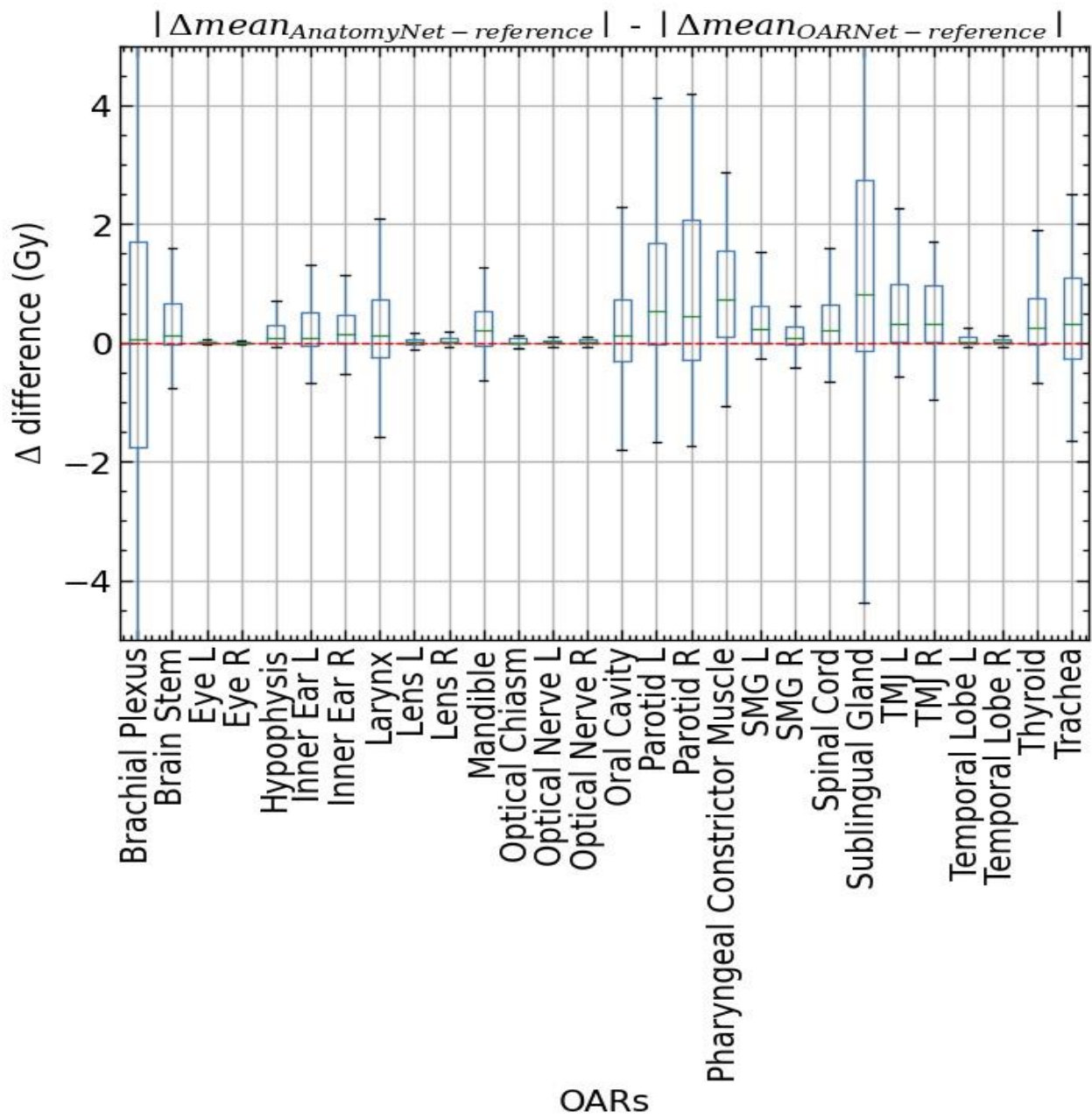


Figure 22 Dosimetric gain or loss for mean doses comparing OARnet with the AnatomyNet for 28 OARs

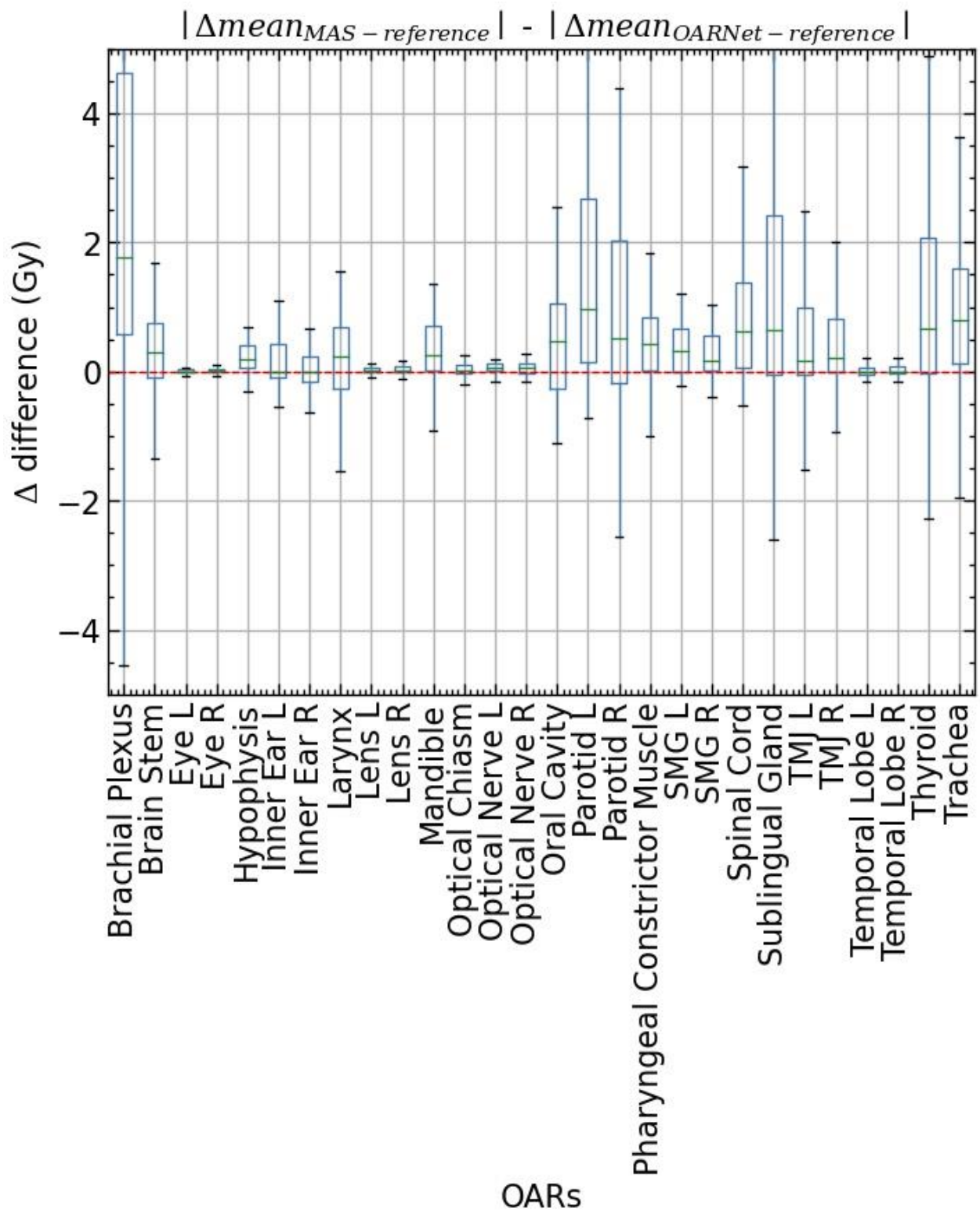


Figure 23 Dosimetric gain or loss for mean doses comparing OARnet with the MAS for 28 OARs

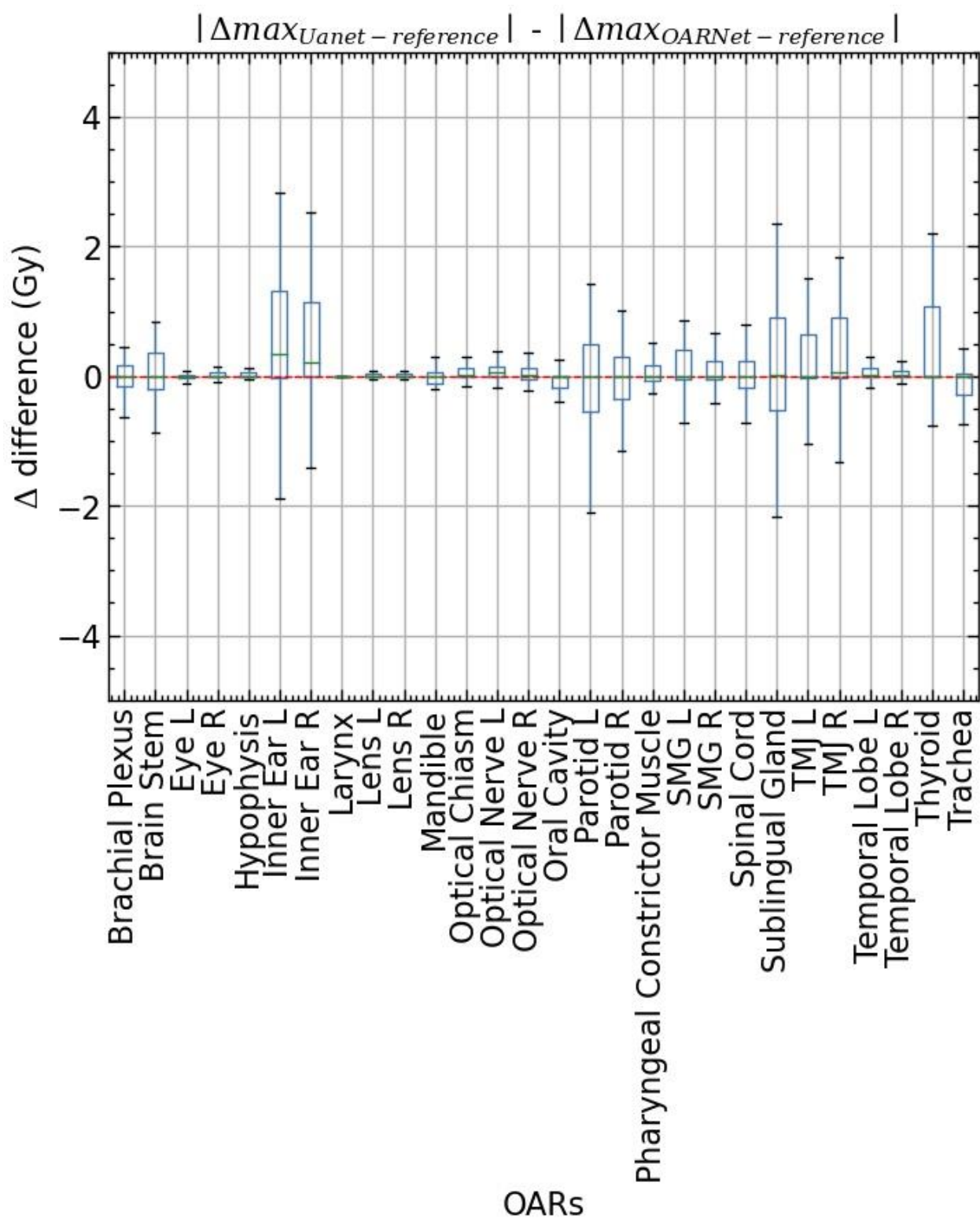


Figure 24 Dosimetric gain or loss for max doses comparing OARnet with the Uanet for 28 OARs

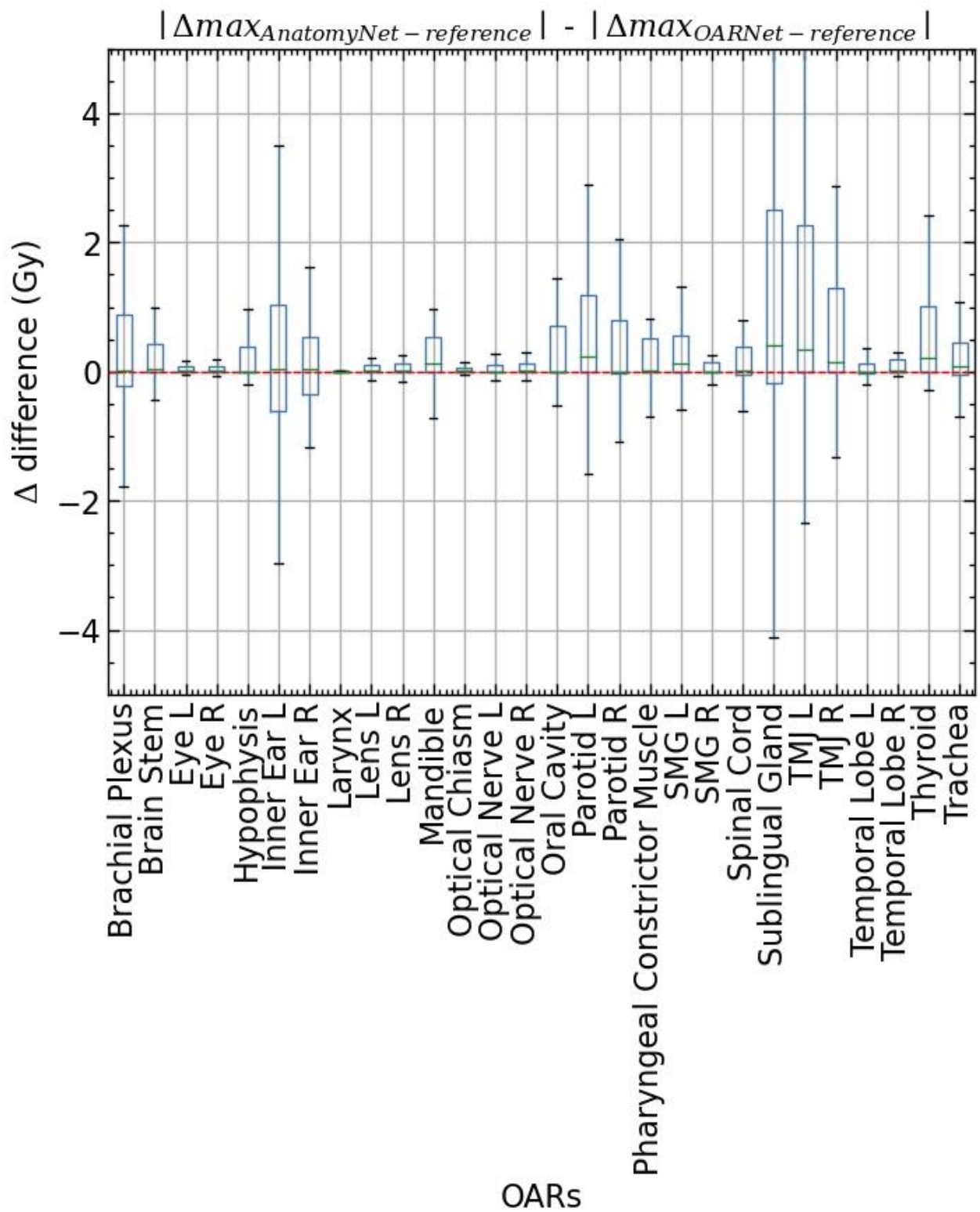


Figure 25 Dosimetric gain or loss for max doses comparing OARnet with the AnatomyNet for 28 OARs

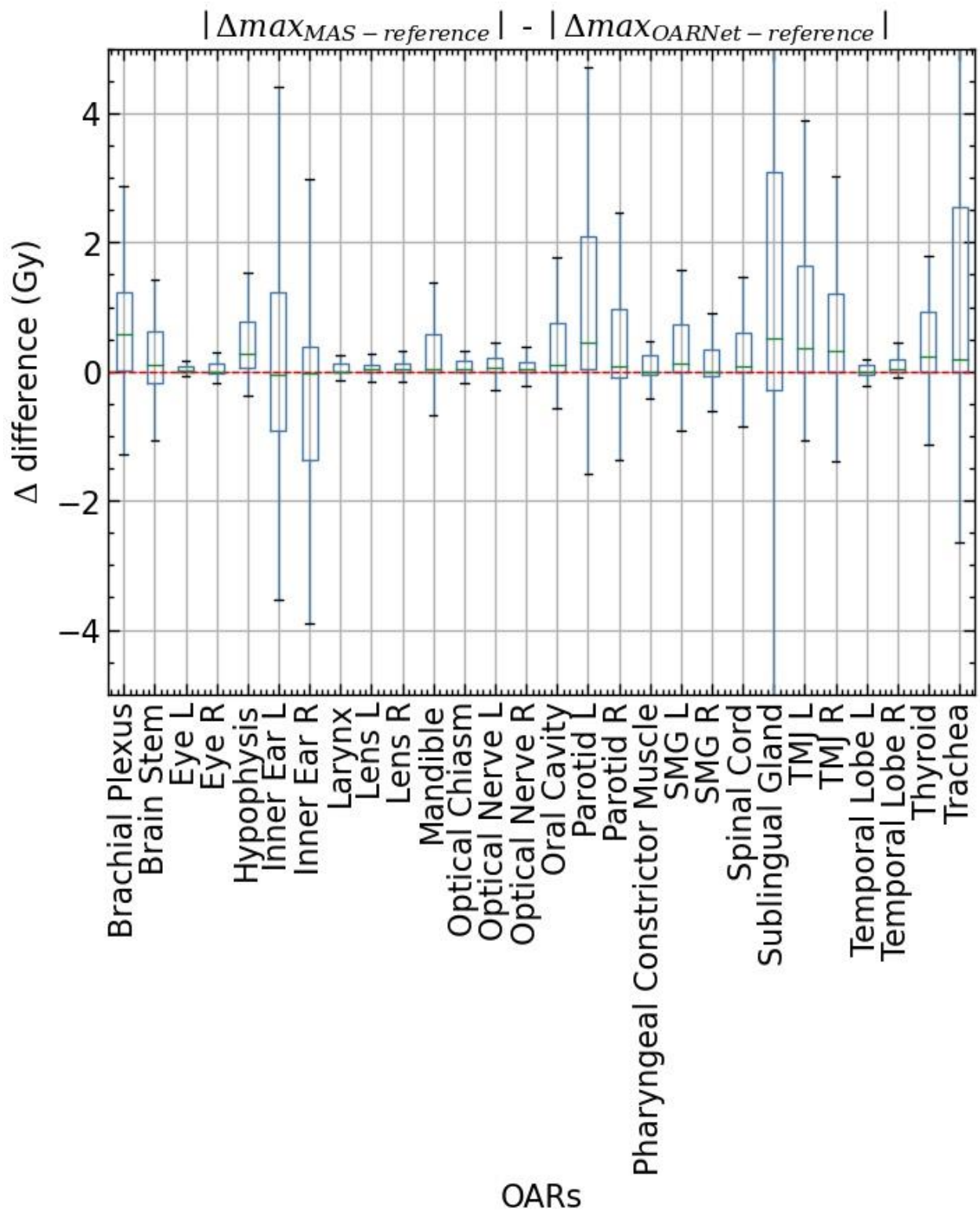


Figure 26 Dosimetric gain or loss for max doses comparing OARnet with the MAS for 28 OARs